

Journal Pre-proof

Comparison of beamformer implementations for MEG source localization

Amit Jaiswal, Jukka Nenonen, Matti Stenroos, Alexandre Gramfort, Sarang S. Dalal, Britta U. Westner, Vladimir Litvak, John C. Mosher, Jan-Mathijs Schoffelen, Caroline Witton, Robert Oostenveld, Lauri Parkkonen



PII: S1053-8119(20)30284-6

DOI: <https://doi.org/10.1016/j.neuroimage.2020.116797>

Reference: YNIMG 116797

To appear in: *NeuroImage*

Received Date: 3 October 2019

Revised Date: 18 February 2020

Accepted Date: 31 March 2020

Please cite this article as: Jaiswal, A., Nenonen, J., Stenroos, M., Gramfort, A., Dalal, S.S., Westner, B.U., Litvak, V., Mosher, J.C., Schoffelen, J.-M., Witton, C., Oostenveld, R., Parkkonen, L., Comparison of beamformer implementations for MEG source localization, *NeuroImage*, <https://doi.org/10.1016/j.neuroimage.2020.116797>.

This is a PDF file of an article that has undergone enhancements after acceptance, such as the addition of a cover page and metadata, and formatting for readability, but it is not yet the definitive version of record. This version will undergo additional copyediting, typesetting and review before it is published in its final form, but we are providing this version to give early visibility of the article. Please note that, during the production process, errors may be discovered which could affect the content, and all legal disclaimers that apply to the journal pertain.

© 2020 Published by Elsevier Inc.

1 Comparison of beamformer implementations for MEG source 2 localization

3 Amit Jaiswal^{1,2}, Jukka Nenonen¹, Matti Stenroos², Alexandre Gramfort³, Sarang S. Dalal⁴, Britta U. Westner⁴,
4 Vladimir Litvak⁵, John C. Mosher⁶, Jan-Mathijs Schoffelen⁷, Caroline Witton⁹, Robert Oostenveld^{7,8}, Lauri
5 Parkkonen^{1,2}

6 ¹Megin Oy¹, Helsinki, Finland.

7 ²Department of Neuroscience and Biomedical Engineering, Aalto University School of Science, Espoo,
8 Finland

9 ³Université Paris-Saclay, Inria, CEA, Palaiseau, France

10 ⁴Center of Functionally Integrative Neuroscience, Aarhus University, Denmark

11 ⁵The Wellcome Centre for Human Neuroimaging, UCL Queen Square Institute of Neurology, London, UK

12 ⁶Department of Neurology, University of Texas Health Science Center at Houston, Houston, Texas, USA

13 ⁷Donders Institute for Brain, Cognition and Behaviour, Radboud University, Nijmegen, The Netherlands

14 ⁸NatMEG, Karolinska Institutet, Stockholm, Sweden

15 ⁹Aston Brain Centre, School of Life and Health Sciences, Aston University, Birmingham, UK

16

17 Abstract

18 Beamformers are applied for estimating spatiotemporal characteristics of neuronal sources
19 underlying measured MEG/EEG signals. Several MEG analysis toolboxes include an
20 implementation of a linearly constrained minimum-variance (LCMV) beamformer. However,
21 differences in implementations and in their results complicate the selection and application of
22 beamformers and may hinder their wider adoption in research and clinical use. Additionally,
23 combinations of different MEG sensor types (such as magnetometers and planar gradiometers)
24 and application of preprocessing methods for interference suppression, such as signal space
25 separation (SSS), can affect the results in different ways for different implementations. So far, a
26 systematic evaluation of the different implementations has not been performed. Here, we
27 compared the localization performance of the LCMV beamformer pipelines in four widely used
28 open-source toolboxes (MNE-Python, FieldTrip, DAiSS (SPM12), and Brainstorm) using datasets
29 both with and without SSS interference suppression.

30 We analyzed MEG data that were i) simulated, ii) recorded from a static and moving phantom, and
31 iii) recorded from a healthy volunteer receiving auditory, visual, and somatosensory stimulation.
32 We also investigated the effects of SSS and the combination of the magnetometer and
33 gradiometer signals. We quantified how localization error and point-spread volume vary with the
34 signal-to-noise ratio (SNR) in all four toolboxes.

¹ Former name: Elekta Oy

35 When applied carefully to MEG data with a typical SNR (3–15 dB), all four toolboxes localized the
36 sources reliably; however, they differed in their sensitivity to preprocessing parameters. As
37 expected, localizations were highly unreliable at very low SNR, but we found high localization error
38 also at very high SNRs for the first three toolboxes while Brainstorm showed greater robustness
39 but with lower spatial resolution. We also found that the SNR improvement offered by SSS led to
40 more accurate localization.

41 **Keywords**

42 MEG, EEG, source modeling, beamformers, LCMV, open-source analysis toolbox.

43

44

Journal Pre-proof

45 **1. Introduction**

46 MEG (magnetoencephalography) and EEG (electroencephalography) source imaging aims to
47 identify the spatiotemporal characteristics of neural source currents based on the recorded signals,
48 electromagnetic forward models and physiologically motivated assumptions about the source
49 distribution. One well-known method for estimating a small number of focal sources is to model
50 each of them as a current dipole with fixed location and fixed or changing orientation. The locations
51 (optionally orientations) and time courses of the dipoles are then collectively estimated (Mosher et
52 al., 1992; Hämäläinen et al., 1993). Such equivalent dipole models have been widely applied in
53 basic research (see e.g. Salmelin, 2010) as well as in clinical practice (Bagic et al., 2011a; 2011b;
54 Burgess et al., 2011). Distributed source imaging estimates source currents distribution across the
55 whole source space, typically the cortical surface. Examples of linear methods for distributed
56 source estimation are LORETA (low-resolution brain electromagnetic tomography; Pascual-Marqui
57 et al., 1994) and MNE (minimum-norm estimation; Hämäläinen and Ilmoniemi, 1994). From
58 estimated source distributions, one often computes noise-normalized estimates such as dSPM
59 (dynamic statistical parametric mapping; Dale et al., 2000). Also, various non-linear distributed
60 inverse methods have been proposed (Wipf et al., 2010; Gramfort et al., 2013b).

61 While dipole modeling and distributed source imaging estimate source distributions that reconstruct
62 (the relevant part of) the measurement, beamforming takes an adaptive spatial-filtering approach,
63 scanning independently each location in a predefined region of interest (ROI) within the source
64 space without attempting to reconstruct the data. LCMV beamforming can be done in time or
65 frequency domain; time-domain methods (Van Veen and Buckley, 1988; 1997; Spencer et al.,
66 1992; Sekihara et al., 2006) use covariance matrices whereas frequency domain methods, such as
67 DICS (Dynamic Imaging of Coherent Sources; Gross et al., 2001), utilizes cross-spectral density
68 matrices. There are also other variants of beamformer for MEG source imaging, such as SAM
69 (Synthetic Aperture Magnetometry; Robinson and Vrba, 1998) and SAM-based ERB (Event-related
70 Beamformer; Cheyne et al., 2007) etc. They differ slightly in covariance computation, forward
71 model selection, optimal orientation search, and weight normalization of the output power.

72 The LCMV beamformer estimates the activity for a source at a given location (typically a point
73 source) while simultaneously suppressing the contributions from all other sources and noise
74 captured in the data covariance matrix. For evaluation of the spatial distribution of the estimated
75 source activity, an image is formed by scanning a set of predefined possible source locations and
76 computing the beamformer output (often power) at each location in the scanning space. When the
77 scanning is done in a volume grid, the beamformer output is typically presented by superimposing
78 it onto an anatomical MRI.

79 There are two main categories of beamformers applied in the MEG/EEG source analysis— vector
80 type and scalar type. Vector beamformers consider all source orientations while scalar

81 beamformers use either a predefined source orientation or they try to find the maximum output
82 power projection. Spatial resolution of scalar beamformers is higher than that of the vector type
83 (Vrba and Robinson, 2000; Hillebrand and Barnes, 2003).

84 Beamformers have been popular in basic MEG research studies (e.g. Hillebrand and Barnes,
85 2005; Braca et al., 2011; Ishii et al., 2014; van Es and Schoffelen, 2019) as well as in clinical
86 applications such as in localization of epileptic events (e.g. Mohamed et al., 2013; Van Klink et al.,
87 2017; Youssofzadeh et al., 2018; Hall et al., 2018). Many variants of beamformers are
88 implemented in several open-source toolboxes and commercial software for MEG/EEG analysis.
89 Presently, based on citation counts, the most used open-source toolboxes for MEG data analysis
90 are FieldTrip (Oostenveld et al., 2011), Brainstorm (Tadel et al., 2011), MNE-Python (Gramfort et
91 al., 2013a) and DAiSS in SPM12 (Litvak et al., 2011). These four toolboxes have an
92 implementation of an LCMV beamformer, based on the same theoretical framework (van Veen et
93 al., 1997; Sekihara et al., 2006). Yet, it has been anecdotally reported that these toolboxes may
94 yield different results for the same data. These differences may arise not only from the core of the
95 beamformer implementation but also from the previous steps in the analysis pipeline, including
96 data import, preprocessing, forward model computation, combination of data from different sensor
97 types, covariance estimation, and regularization method. Beamforming results obtained from the
98 same toolbox may also differ substantially depending on the applied preprocessing methods; for
99 example, Signal Space Separation (SSS; Taulu and Kajola 2005) reduces the rank of the data,
100 which could affect beamformer output unpredictably if not appropriately considered in the
101 implementation.

102 In this study, we evaluated the LCMV beamformer pipelines in the four open-source toolboxes and
103 investigated the reasons for possible inconsistencies, which hinder the wider adoption of
104 beamformers to research and clinical use where accurate localization of sources is required, e.g.,
105 in pre-surgical evaluation. These issues motivated us to study the conditions in which these
106 toolboxes succeed and fail to provide systematic results for the same data and to investigate the
107 underlying reasons.

108

109 **2. Materials and Methods**

110 **2.1. Datasets**

111 To compare the beamformer implementations, we employed MEG data obtained from simulations,
112 phantom measurements, and measurements of a healthy volunteer who received auditory, visual,
113 and somatosensory stimuli. For all human data recordings, informed consent was obtained from all
114 study subjects in agreement with the approval of the local ethics committee.

115 **2.1.1. MEG systems**

116 All MEG recordings were performed in a magnetically shielded room with a 306-channel MEG
117 system (either Elekta Neuromag® or TRIUX™; Megin Oy, Helsinki, Finland), which samples the
118 magnetic field distribution by 510 coils at distinct locations above the scalp. The coils are
119 configured into 306 independent channels arranged on 102 triple-sensor elements, each housing a
120 magnetometer and two perpendicular planar gradiometers. The location of the phantom or
121 subject's head relative to the MEG sensor array was determined using four or five head position
122 indicator (HPI) coils attached to the scalp. A Polhemus Fastrak® system (Colchester, VT, USA)
123 was used for digitizing three anatomical landmarks (nasion, left and right preauricular points) to
124 define the head coordinate system. Additionally, the centers of the HPI coils and a set of ~50
125 additional points defining the scalp were also digitized. The head position in the MEG helmet was
126 determined at the beginning of each measurement using the 'single-shot' HPI procedure, where
127 the coils are activated briefly, and the coil positions are estimated from the measured signals. The
128 location and orientation of the head with respect to the helmet can then be calculated since the coil
129 locations were known both in the head and in the device coordinate systems. After this initial head
130 position measurement, continuous tracking of head movements (cHPI) was engaged by keeping
131 the HPI coils activated to track the movement continuously.

132 **2.1.2. Simulated MEG data**

133 To obtain realistic MEG data with known sources, we superimposed simulated sensor signals
134 based on forward modeling of dipolar sources onto measured resting-state MEG data utilizing a
135 special in-house simulation software. Structural MRI images, acquired from a healthy adult
136 volunteer using a 3-tesla MRI scanner (Siemens Trio, Erlangen, Germany), were segmented using
137 the MRI Segmentation Software of Megin Oy (Helsinki, Finland) and the surface enveloping the
138 brain compartment was tessellated with triangles (5-mm side length). Using this mesh, a realistic
139 single-shell volume conductor model was constructed using the Boundary Element Method (BEM;
140 Hämäläinen and Sarvas, 1989) implemented in the Source modeling software of Megin Oy. We
141 also segmented the cortical mantle with the FreeSurfer software (Dale et al., 1999; Fischl et al.,
142 1999; Fischl, 2012) for deriving a realistic source space. By using the "ico4" subdivision in MNE-

143 Python, we obtained a source space comprising 2560 dipoles (average spacing 6.2 mm) in each
144 hemisphere (Fig. 1a). Out of these, we selected 25 roughly uniformly distributed source locations in
145 the left hemisphere for the simulations (Fig. 1a). All these points were at least 7.5 mm inwards from
146 the surface of the volume conductor model. Using the conductor model, source locations and
147 sensor locations from the resting-state data in MNE-Python, we simulated dipoles at each of the 25
148 locations – one at a time – with a 10-Hz sinusoid of 200-ms duration (2 cycles). The dipoles were
149 simulated at eight source amplitudes: 10, 30, 80, 200, 300, 450, 600 and 800 nAm and sensor-
150 level evoked field data were computed. Fig. 1b shows a few of the simulated evoked responses
151 (whitened with noise) at a single dipole location but at different strengths, illustrating the changes in
152 the signal-to-noise ratio (SNR). Here t_{max} is the time point of the SNR estimate, which is defined
153 later in Section 2.5.

154

155

156

Insert Fig.1 about here

157

158 The continuous resting-state MEG data with eyes open was recorded from the same volunteer who
159 provided the anatomical data, using an Elekta Neuromag® MEG system (at BioMag Laboratory,
160 Helsinki, Finland). The recording length was 2 minutes, the sampling rate was 1 kHz, and the
161 acquisition frequency band was 0.1–330 Hz. This recording provided the head position for the
162 simulations and defined their noise characteristics. MEG and MRI data were co-registered using
163 the digitized head shape points and the outer skin surface in the segmented MRI.

164 The simulated sensor-level evoked fields data were superimposed on the unprocessed resting-
165 state recording with inter-trial-interval varying between 1000–1200 ms resulting in ~110 trials
166 (epochs) in each simulated dataset. The resting-state recording was used both as raw without
167 preprocessing and after SSS interference suppression. Altogether, we obtained 400 simulated
168 MEG datasets (25 source locations at 8 dipole amplitudes, all both with the raw and SSS-
169 preprocessed real data). Fig. 2 illustrates the generation of simulated MEG data.

170

171

Insert Fig. 2 about here

172 **2.1.3. Phantom data**

173 We used a commercial MEG phantom (Megin Oy, Helsinki, Finland) which contains 32 dipoles and
174 4 HPI coils at distinct fixed locations (see Fig 3a–c and TRIUX™ User's Manual, Megin Oy). The
175 phantom is based on the triangle construction (Ilmoniemi et al., 1985): an isosceles triangular line

176 current generates on its relatively very short side a magnetic field distribution equivalent to that of a
177 tangential current dipole in a spherical conductor model, provided that the vertex of the triangle and
178 the origin of the model of a conducting sphere coincide. The phantom data were recorded from 8
179 dipoles, excited one by one, using a 306-channel TRIUXTM system (at Aston University,
180 Birmingham, UK). The distance from the phantom origin was 64 mm for dipoles 5 and 9 (the
181 shallowest), 54 mm for dipoles 6 and 10, 44 mm for dipoles 7 and 11, and 34 mm for dipoles 8 and
182 12 (the deepest; see Fig 3c). The phantom was first kept stationary inside the MEG helmet and
183 continuous MEG data were recorded with 1-kHz sampling rate for three dipole amplitudes (20, 200
184 and 1000 nAm); one dipole at a time was excited with a 20-Hz sinusoidal current for 500 ms,
185 followed by 500 ms of inactivity. The recordings were repeated with the 200-nAm dipole strength
186 while moving the phantom continuously to mimic head movements inside the MEG helmet. The
187 experimenter made sequences of continuous random rotational and translational movements by
188 holding the phantom rod and keeping the phantom (hemispheric structure) inside the helmet,
189 followed by periods without movement; see the movements in Fig. 3e and Suppl. Fig. 2 for all
190 movement parameters.

191

192

Insert Fig. 3 about here

193

194 **2.1.4. Human MEG data**

195 We recorded MEG evoked responses from the same volunteer whose MRI and spontaneous MEG
196 data were utilized in the simulations. These human data were recorded using a 306-channel Elekta
197 Neuromag® system (at BioMag Laboratory, Helsinki, Finland). During the MEG acquisition, the
198 subject was receiving a random sequence of visual (a checkerboard pattern in one of the four
199 quadrants of the visual field), somatosensory (electric stimulation of the median nerve at the
200 left/right wrist at the motor threshold) and auditory (1-kHz 50-ms tone pips to the left/right ear)
201 stimuli with an interstimulus interval of ~500 ms. The Presentation software (Neurobehavioral
202 Systems, Inc., Albany, CA, USA) was used to produce the stimuli.

203 **2.2. Preprocessing**

204 The datasets were analyzed in two ways: 1) omitting bad channels from the analysis, without
205 applying SSS preprocessing, and 2) applying SSS-based preprocessing methods (SSS/tSSS) to
206 reduce magnetic interference and perform movement compensation for moving phantom data. The
207 SSS-based preprocessing and movement compensation were performed in MaxFilterTM software
208 (version 2.2; MEGIN Oy, Helsinki, Finland). After that, the continuous data were bandpass filtered
209 (passband indicated for each dataset later in the text) followed by the removing of the dc. Then the

210 data were epoched to trials around each stimulus. We applied an automatic trial rejection
 211 technique based on the maximum variance across all channels, rejecting trials that had variance
 212 higher than the 98th percentile of the maximum or lower than the 2nd percentile (see Suppl. Fig. 4).
 213 This method is available as an optional preprocessing step in FieldTrip, and the same
 214 implementation was applied in the other toolboxes. For each dataset, the covariance matrices
 215 (data or noise) were calculated over each trial and normalized by the total number of samples
 216 across the trials:

$$217 \quad C = \frac{\sum_{i=1}^j C_i}{N_s} \quad (1)$$

218 where C is the resulting data or noise covariance, j is the total number of good trials after
 219 covariance-based trial rejection, C_i is the covariance matrix of i^{th} trial and N_s is the total number of
 220 samples used in computing all C_i matrices. Below we describe the detailed preprocessing steps for
 221 all datasets.

222 **2.2.1. Simulated data**

223 In each toolbox, the raw data with just bad channels removed or SSS-preprocessed continuous
 224 data were filtered using a zero-phase filter with a passband of 2–40 Hz. The filtered data were
 225 epoched into windows from –200 to +200 ms relative to the start of the source activity. The bad
 226 epochs were removed using the variance-based automatic trial rejection technique, resulting in
 227 ~100 epochs. Then using Eq (1), the noise and data covariance matrices were estimated from
 228 these epochs for the time windows of –200 to –20 ms and 20 to 200 ms, respectively.

229 **2.2.2. Phantom data**

230 All 32 datasets (static: 3 dipole strengths and 8 dipole locations; moving: 1 dipole strength and 8
 231 dipole locations) were analyzed both without and with SSS-preprocessing. We applied SSS on
 232 static phantom data to remove external interference. On moving-phantom data, combined temporal
 233 SSS and movement compensation (tSSS_mc) were applied for suppressing external and
 234 movement-related interference and for transforming the data from the continuously estimated
 235 positions into a static reference position (Taulu and Kajola 2005; Nenonen et al., 2012). Then in
 236 each toolbox the continuous data were filtered to 2–40 Hz using a zero-phase bandpass filter, and
 237 the filtered data were epoched from –500 to +500 ms with respect to stimulus triggers. Bad epochs
 238 were removed using the automated method based on maximum variance, yielding ~100 epochs for
 239 each dataset. The noise and data covariance matrices were estimated using Eq (1) in each toolbox
 240 for the time windows of –500 to –50 ms and 50 to 500 ms, respectively.

241 **2.2.3. Human MEG data**

242 Both the unprocessed raw data and the data preprocessed with tSSS were filtered to 1–95 Hz
243 using a zero-phase bandpass filter in each toolbox. The trials with somatosensory stimuli (SEF)
244 were epoched between –100 to –10 and 10 to 100 ms for estimating the noise and data
245 covariances, respectively. The corresponding time windows for the auditory-stimulus trials (AEF)
246 were –150 to –20 and 20 to 150 ms, and for the visual stimulus trials (VEF) –200 to –50 and 50 to
247 200 ms, respectively. Trials contaminated by excessive eye blinks (EOG > 250 μ V) or by excessive
248 magnetic signals (MEG > 5000 fT or 3000 fT/cm) were removed with the variance-based
249 automated trial removal technique. Before covariance computation, baseline correction by the time
250 window before the stimulus was applied on each trial. The covariance matrices were estimated
251 independently in each toolbox, using Eq (1).

252 Since the actual source locations associated with the evoked fields are not precisely known, we
253 defined reference locations using conventional dipole fitting in the Source Modelling Software of
254 Megin Oy (Helsinki, Finland). A single equivalent dipole was used to represent SEF and VEF
255 sources, and one dipole per hemisphere was used for AEF (see Suppl. Fig. 3). The dipole fitting
256 was performed at the time point of the maximum RMS value across all planar gradiometer
257 channels (global field power) of the average response amplitude.

258 **2.2.4. Forward model**

259 For the beamformer scan of simulated data, we used the default or the most commonly used
260 forward model of each toolbox: a single-compartment BEM model in MNE-Python, a single-shell
261 corrected-sphere model (Nolte, 2003) in FieldTrip, a single-shell corrected sphere model (Nolte,
262 2003) through inverse normalization of template meshes (Mattout et al., 2007) in DAiSS (SPM12),
263 and the overlapping-spheres (Huang et al., 1999) model in Brainstorm. The former three packages
264 utilize inner skull for defining the boundary of the models. For constructing the models for the
265 forward solutions, the segmentation of MRI images was performed in FreeSurfer for MNE-Python
266 and Brainstorm while FieldTrip and SPM12 used the SPM segmentation procedure. In MNE-
267 Python, FieldTrip and SPM12, a volumetric source space was represented by a rectangular grid
268 with 5-mm resolution enclosed by the conductor models in these packages while Brainstorm uses
269 a rectangular grid with the same resolution enclosed by the brain surface. Since each toolbox
270 prepares a head model and source space using slightly different methods, these models may differ
271 from each other. Fig. 4 shows the small discrepancies in the boundary of source spaces used by
272 the three packages. These discrepancies may result in a small shift between the positions and
273 number of the scanning points in these toolboxes. Forward solutions were computed separately in
274 each toolbox using the head model, the volumetric grid sources, and sensor information from the
275 MEG data.

276

277

Insert Fig. 4 about here

278

279 For phantom data, a homogeneous spherical volume conductor model was defined in each toolbox
 280 with the origin at the head coordinate system origin. An equidistant rectangular source-point grid
 281 with 5-mm resolution was placed inside the upper half of a sphere covering all 32 dipoles of the
 282 phantom; see Fig. 3d. Forward solutions for these grids were computed independently in each
 283 toolbox. For human MEG data, the head models and the source space were defined in the same
 284 way as for the beamformer scanning of the simulated data.

285 2.3. LCMV beamformer

286 The linearly constrained minimum-variance (LCMV) beamformer is a spatial filter that relates the
 287 magnetic field measured outside the head to the underlying neural activities using the covariance
 288 of measured signals and models of source activity and signal transfer between the source and the
 289 sensor (Spencer et al., 1992; van Veen et al. 1997; Robinson and Vrba, 1998). The spatial filter
 290 weights are computed for each location in the region of interest (ROI).

291 Let \mathbf{x} be an $M \times 1$ signal vector of MEG data measured with M sensors, and N is the number of
 292 grid points in the ROI with grid locations r_j , ($j = 1, \dots, N$). Then the source $\mathbf{y}(r_j)$ at any location r_j
 293 can be estimated as weighted combination of the measurement \mathbf{x} as

$$294 \quad \mathbf{y}(r_j) = \mathbf{W}^T(r_j)\mathbf{x} \quad (2)$$

295 where the $M \times 3$ matrix $\mathbf{W}(r_j)$ is known as spatial filter for a source at location r_j . This type of
 296 spatial filter provides a *vector type beamformer* by separately estimating the activity for three
 297 orthogonal source orientations, corresponding to the three columns of the matrix. According to Eqs
 298 16–23 in van Veen et al. (1997), the spatial filter $\mathbf{W}(r_j)$ for vector beamformer is defined as

$$299 \quad \mathbf{W}(r_j) = \left(\mathbf{L}^T(r_j)\mathbf{C}^{-1}\mathbf{L}(r_j) \right)^{-1} \mathbf{L}^T(r_j)\mathbf{C}^{-1} \quad (3)$$

300 Here $\mathbf{L}(r_j)$ is the $M \times 3$ local leadfield matrix that defines the contribution of a dipole source at
 301 location r_j in the measured data \mathbf{x} , and \mathbf{C} is the covariance matrix computed from the measured
 302 data samples. To perform source localization using LCMV, the output variance (or output source
 303 power) $\text{Var}(\mathbf{y}(r_j))$ is estimated at each point in the source space (see Eq (24) in van Veen et al.,
 304 1997), resulting in

$$305 \quad \widehat{\text{Var}}(\mathbf{y}(r_j)) = \text{Trace}[\mathbf{L}^T(r_j)\mathbf{C}^{-1}\mathbf{L}(r_j)]^{-1} \quad (4)$$

306 Usually, the measured signal is contaminated by non-uniformly distributed noise and therefore the
 307 estimated signal variance is often normalized with projected noise variance \mathbf{C}_n calculated over
 308 some baseline data (noise). Such normalized estimate is called Neural Activity Index (NAI; van
 309 Veen et al., 1997) and can be expressed as

$$310 \quad \text{NAI}(r_j) = \text{Trace}\left\{\left[\mathbf{L}^T(r_j)\mathbf{C}^{-1}\mathbf{L}(r_j)\right]^{-1}\right\} / \text{Trace}\left\{\left[\mathbf{L}^T(r_j)\mathbf{C}_n^{-1}\mathbf{L}(r_j)\right]^{-1}\right\} \quad (5)$$

311 Scanning over all the locations in the region of interest in source space transforms the MEG data
 312 from a given measurement into an NAI map.

313 In contrast to a vector beamformer, a *scalar beamformer* (Sekihara and Scholz, 1996; Robinson
 314 and Vrba, 1998) uses constant source orientation that is either pre-fixed or optimized from the
 315 input data by finding the orientation that maximizes the output source power at each target
 316 location. Besides simplifying the output, the optimal-orientation scalar beamformer enhances the
 317 output SNR compared to the vector beamformer (Robinson and Vrba, 1998; Sekihara et al., 2004).
 318 The optimal orientation $\boldsymbol{\eta}_{\text{opt}}(r_j)$, for location r_j can be determined by generalized eigenvalue
 319 decomposition (Sekihara et al., 2004) using Rayleigh–Ritz formulation as

$$320 \quad \boldsymbol{\eta}_{\text{opt}}(r_j) = \mathbf{v}_{\min}\left\{\mathbf{L}^T(r_j)\mathbf{C}^{-2}\mathbf{L}(r_j), \mathbf{L}^T(r_j)\mathbf{C}^{-1}\mathbf{L}(r_j)\right\} \quad (6)$$

321 where \mathbf{v}_{\min} indicates the eigenvector corresponding to the smallest generalized eigenvalue of the
 322 matrices enclosed in Eq (6) curly braces. For further details, see Eq (4.44) and Section 13.3 in
 323 Sekihara and Nagarajan (2008).

324 Denoting $\mathbf{I}_{\boldsymbol{\eta}_{\text{opt}}}(r_j) = \mathbf{L}(r_j)\boldsymbol{\eta}_{\text{opt}}(r_j)$ instead of $\mathbf{L}(r_j)$, the weight matrix in Eq (3) becomes $M \times 1$
 325 weight vector $\mathbf{w}(r_j)$,

$$326 \quad \mathbf{w}(r_j) = \left(\mathbf{I}_{\boldsymbol{\eta}_{\text{opt}}}^T(r_j)\mathbf{C}^{-1}\mathbf{I}_{\boldsymbol{\eta}_{\text{opt}}}(r_j)\right)^{-1} \mathbf{I}_{\boldsymbol{\eta}_{\text{opt}}}^T(r_j)\mathbf{C}^{-1} \quad (7)$$

327 Using $\mathbf{I}_{\boldsymbol{\eta}_{\text{opt}}}(r_j)$ in Eq (5), we find the estimate (NAI) of a scalar LCMV beamformer as

$$328 \quad \text{NAI}(r_j) = \mathbf{I}_{\boldsymbol{\eta}_{\text{opt}}}^T(r_j)\mathbf{C}_n^{-1}\mathbf{I}_{\boldsymbol{\eta}_{\text{opt}}}(r_j) / \mathbf{I}_{\boldsymbol{\eta}_{\text{opt}}}^T(r_j)\mathbf{C}^{-1}\mathbf{I}_{\boldsymbol{\eta}_{\text{opt}}}(r_j) \quad (8)$$

329 When the data covariance matrix is estimated from a sufficiently large number of samples and it
 330 has full rank, Eq (8) provides the maximum spatial resolution (Lin et al., 2008; Sekihara and
 331 Nagarajan, 2008). According to van Veen and colleagues (1997), the number of samples for
 332 covariance estimation should be at least three times the number of sensors. Thus, sometimes, the
 333 amount of available data may be insufficient to obtain a good estimate of the covariance matrices.
 334 In addition, pre-processing methods such as signal-space projection (SSP) or signal-space
 335 separation (SSS) reduce the rank of the data, which impacts the matrix inversions in Eq (8). These
 336 problems can be mitigated using Tikhonov regularization (Tikhonov, 1963) by replacing matrix \mathbf{C}^{-1}
 337 by its regularized version $(\mathbf{C} + \lambda\mathbf{I})^{-1}$ in Eqs (3–8) where λ is called the regularization parameter.

338 All tested toolboxes set the λ with respect to the mean data variance, using ratio 0.05 as default:

339 $\lambda = 0.05 \times \text{Trace}(\mathbf{C})/M$.

340 If the data are not full rank, also the noise covariance matrix \mathbf{C}_n needs to be regularized.

341

342 **2.4. Differences between the beamformer pipelines**

343 Though all the four toolboxes evaluated here use the same theoretical framework of the LCMV
344 beamformer, there are several implementation differences which might affect the exact outcome of
345 a beamformer analysis pipeline. Many of these differences pertain to specific handling of the data
346 prior to the estimation of the spatial filters, or to specific ways of (post)processing the beamformer
347 output. Some of the toolbox-specific features reflect the characteristics of the MEG system around
348 which the toolbox has evolved. Importantly, some of these differences are sensitive to input SNR,
349 and they can lead to differences in the results. Table 1 lists the main characteristics and settings of
350 the four toolboxes used in this study. We used the default settings of each toolbox (general
351 practice) for steps before beamforming but set the actual beamforming steps as similar as possible
352 across the toolboxes to be able to meaningfully compare the results.

353

Insert Table 1 about here

354 All toolboxes import data using either Matlab or Python import functions of the MNE software
355 (Gramfort et al., 2014) but represent the data internally either in T or fT (magnetometer) and T/m or
356 fT/mm (gradiometer); see Suppl. Fig. 5. Default filtering approaches across toolboxes change the
357 numeric values, so the linear correlation between the same channels across toolboxes deviates
358 from the identity line; see Suppl. Fig. 6. The default head model is also different across toolboxes;
359 see Section 2.2.4. The single-shell BEM and single-shell corrected sphere model (the “Nolte
360 model”) are approximately as accurate but produce slightly different results (Stenroos et al., 2014).

361 For MEG–MRI co-registration, there are several approaches available across these toolboxes such
362 as an interactive method using fiducial or/and digitization points defining the head surface, using
363 automated point cloud registration methods e.g., the iterative closest point (ICP) algorithm. Despite
364 using the same source-space specifications (rectangular grid with 5-mm resolution), differences in
365 head models and/or co-registration methods change the forward model across toolboxes; see
366 Fig. 4. Though there are several approaches to compute data and noise covariances across the
367 four beamformer implementations, by default they all use the empirical/sample covariance. In
368 contrast to other toolboxes, Brainstorm eliminates the cross-modality terms from the data and
369 noise covariance matrices. Also, the regularization parameter λ is calculated and applied

370 separately for gradiometers and magnetometers channel sets in Brainstorm therefore, the same
371 amount of regularization affects differently.

372 The combination of two MEG sensor types in the MEGIN triple-sensor array causes additional
373 processing differences in comparison to other MEG systems that employ only axial gradiometers
374 or only magnetometers. Magnetometers and planar gradiometers have different dynamic ranges
375 and measurement units, so their combination must be appropriately addressed in source analysis
376 such as beamforming. For handling the two sensor types in the analysis, different strategies are
377 used for bringing the channels into the same numerical range. MNE-Python and Brainstorm use
378 pre-whitening (Engemann et al., 2015; Ilmoniemi and Sarvas, 2019) based on noise covariance
379 while FieldTrip and SPM12 assume a single sensor type for all the MEG channels. This approach
380 makes SPM12 to favor magnetometer data (with higher numeric values of magnetometer
381 channels) and FieldTrip to favor gradiometer data (with higher numeric values of gradiometer
382 channels). However, users of FieldTrip and SPM12 usually employ only one channel type of the
383 triple-sensor array for beamforming (most commonly, the gradiometers). Due to the presence of
384 two different sensor types in the MEGIN systems and the potential use of SSS methods, the
385 eigenspectra of data from these systems can be idiosyncratic (see Suppl. Fig. 7) and differ from
386 the single-sensor type MEG systems. Rank deficiency and related phenomena are potential
387 sources of beamforming failures with data that have been cleaned with a method such as SSS.
388 Rank deficiency affects also other MEG sensor arrays using only magnetometers or axial
389 gradiometers when the data are pre-processed with interference suppression methods such as
390 SSP and (t)SSS.

391 Previous studies have shown that the scalar beamformer yields twofold higher output SNR
392 compared to the vector-type beamformer, if the source orientation for the scalar beamformer has
393 been optimized according to Eq 6 (Vrba and Robinson, 2000; Sekihara et al., 2004). Most of the
394 beamformer analysis toolboxes have an implementation of optimal-orientation scalar beamformer.
395 In this study, we used the scalar beamformer in MNE-Python, FieldTrip, and SPM12 but a vector-
396 beamformer in Brainstorm since the orientation optimization was not available. To keep the output
397 dimensionality the same across the toolboxes, we linearly summed the three-dimensional NAI
398 values at each source location. The general analysis pipeline used in this study is illustrated in Fig.
399 5.

400 Insert Fig. 5 about here

401

402 **2.5. Metrics used in comparison**

403 In this study, a single focal source could be assumed to underlie the simulated/measured data. In
 404 such studies, accurate localization of the source is typically desired. We calculated two metrics for
 405 comparing the characteristics of the LCMV beamformer results from the four toolboxes: localization
 406 error, and point spread volume. We also analyzed their dependence on input signal-to-noise ratio.

407 **Localization Error (LE):** True source locations were known for the simulated and phantom MEG
 408 data and served as reference locations in the comparisons. Since the exact source locations for
 409 the human subject MEG data were unknown, we applied the location of a single current dipole as a
 410 reference location (see Section 2.1.4 “Human MEG data”). The Source Modelling Software (Megin
 411 Oy, Helsinki, Finland) was used to fit a single dipole for each evoked-response category at the time
 412 point around the peak of the average response providing the maximum goodness-of-fit value. The
 413 beamformer localization error is computed as the Euclidean distance between the estimated and
 414 reference source locations.

415 **Point-Spread Volume (PSV):** An ideal spatial filter should provide a unit response at the actual
 416 source location and zero response elsewhere. Due to noise and limited spatial selectivity, there is
 417 some filter leakage to the nearby locations, which spreads the estimated variance over a volume.
 418 The focality of the estimated source, also called focal width, depends on several factors such as
 419 the source strength, orientation, and distance from the sensors. PSV measures the focality of an
 420 estimate and is defined as the total volume occupied by the source activity above a threshold
 421 value; thus, a smaller PSV value indicates a more focal source estimate. We fixed the threshold to
 422 50% of the highest NAI in all comparisons. In this study, the volume represented by a single source
 423 in any of the four source spaces (5-mm grid spacing) was 125 mm³. To compute PSV, we
 424 computed the number of active voxels above the threshold and multiplied by the volume of a single
 425 voxel.

426 **Signal-to-Noise ratio (SNR):** Beamformer localization error depends on the input SNR, which
 427 varies – among other factors – as a function of source strength and distance of the source from the
 428 sensor array. Therefore, we evaluated beamformer localization errors and PSV as a function of the
 429 input SNR of the evoked field data.

430 We estimated the SNR for each evoked field MEG dataset in MNE-Python using the estimated
 431 noise covariance C_n by discarding the smallest near-zero eigenvalues. The data were whitened
 432 using the noise covariance, and the effective number of sensors (rank) was then calculated as

$$433 \quad M_{\text{eff}} = M - \Sigma \quad (9)$$

434 where M is the number of all MEG channels and Σ is the total number of near-zero eigenvalues σ_n
 435 of C_n .

436 Then the input SNR was calculated as:

$$437 \quad \text{SNR}_{\text{dB}} = 10 \log_{10} \left(\left[\frac{1}{M_{\text{eff}}} \sum_{k=1}^M \mathbf{x}_k^2(t) \right]_{t_{\text{max}}} \right) \quad (10)$$

438 where $x_k(t)$ is the signal of k^{th} sensor from the whitened evoked field data, t_{max} is the time point at
 439 maximum amplitude of whitened data across all channels and M_{eff} is the number of effective
 440 sensors defined in Eq (9). Since the same data were used in all toolboxes, we used the same input
 441 SNR value for all of them. Fig. 1b compares simulated evoked responses and the changes in SNR
 442 for dipoles at different strengths but at the same location.

443

444

445 **2.6. Data and code availability**

446 The codes we wrote to conduct these analyses are publicly available under a repository
 447 <https://zenodo.org/record/3471758> (DOI: 10.5281/zenodo.3471758). The datasets as well as the
 448 specific versions of the four toolboxes used in the study are available at
 449 <https://zenodo.org/record/3233557> (DOI: 10.5281/zenodo.3233557).

450

451 **3. Results**

452 We computed the source localization error (LE) and the point spread volume (PSV) for each NAI
453 estimate across all datasets from LCMV beamformer in all four toolboxes. We plotted the LE and
454 PSV as a function of the input SNR computed according to Eq (10). To differentiate the localization
455 among the implementations, we followed the following color convention: *MNE-Python*: grey;
456 *FieldTrip*: Lavender; *DAiSS (SPM12)*: Mint; and *Brainstorm*: coral.

457 **3.1. Simulated MEG data**

458 Localization errors and PSV values were calculated for all simulated datasets and plotted against
459 the corresponding input SNR. The SNR of all 200 simulated datasets ranged between 0.5 to 25
460 dB. Fig. 6a shows the variation of localization errors over the range of input SNR for the simulated
461 dataset. The localization error goes high for all toolboxes for very low SNR (< 3 dB) signals (e.g. <
462 ~80-nAm or deep sources). The localization error within the input SNR range 3–12 dB is stable
463 and mostly within 15 mm, and SSS preprocessing widens this SNR range of stable performance to
464 3–15 dB. Unexpectedly, we also found high localization error at high SNR (> 15 dB) for the
465 toolboxes other than Brainstorm. Fig. 6b plots PSV values against input SNR for raw and SSS-
466 preprocessed simulated data. For the low SNR signals (usually, weak or deep sources), all the four
467 toolboxes show high PSV values. The spatial resolution is highest for the SNR range ~3–15 dB. For
468 the SNR > ~15 dB (usually, strong or superficial sources) these toolboxes also show high PSV.
469 Fig. 6a–b shows that none of the four toolboxes provides accurate localization for all SNR values
470 and the spatial resolution of LCMV varies over the range of input SNR.

471

472

Insert Fig. 6 about here

473

474

475 **3.2. Static and moving phantom MEG data**

476 In the case of phantom data, the background noise is very low and there is a single source
477 underneath a measurement. Since, both the dipole simulation and beamformer analysis in case of
478 phantom use a homogeneous sphere model that does not introduce any forward model
479 inaccuracy, except the possible small co-registration error. All four toolboxes show high localization
480 accuracy and high resolution for phantom data, if the input SNR is not very low (< ~3 dB).
481 Corresponding results for the static phantom data are presented in Fig. 7a–b. Fig. 7a indicates the
482 localization error clear dependency on input SNR, it shows high localization errors at very low SNR
483 raw data sets. The high error is because of some unfiltered artifacts in raw data which was
484 removed by SSS. After SSS, the beamformer shows localization error under ~5 mm for all the

485 datasets. Fig. 7b shows the beamforming resolution in terms of PSV. The PSV values show a high
486 spatial resolution for the data with SNR > 5 dB.

487

488

Insert Fig. 7 about here

489

490 In the cases of moving phantom, Fig. 8a shows high localization errors with unprocessed raw data
491 because of disturbances caused by the movement. The dipole excitation amplitude was 200 nAm,
492 which is enough to provide a good SNR, but the movement artifacts lower the SNR. The most
493 superficial dipoles (Dipoles 5 and 9 in Fig. 3c) possess higher SNR but also higher localization
494 error since they get more significant angular displacement during movement. Because of
495 differences in implementations and preprocessing parameters listed in Section 2.4, apparent
496 differences among the estimated localization error can be seen. Overall, MNE-Python shows the
497 lowest while DAiSS (SPM12) shows the highest localization error with the phantom data with
498 movement artifact. After applying for spatiotemporal tSSS and movement compensation, the
499 improved SNR provided significantly better localization accuracies for all the toolboxes. Fig. 8b
500 shows the PSV for moving phantom data for raw and processed data. The plots indicate
501 improvement in SNR and spatial resolution after tSSS with movement compensation.

502

503

Insert Fig. 8 about here

504

505 Table 2 lists the mean localization error and PSV for the simulated and static phantom datasets
506 over three ranges of SNR— 1) very low (less than 3 dB) where all the four implementations show
507 unreliable localization and the lowest spatial resolution, 2) feasible range (3–15 dB) that covers
508 most of the research studies where all the four implementations are reliable and robust, and 3)
509 high SNR (above 15 dB) where the source estimation by Brainstorm is comparatively more robust.

510

Insert Table 2 about here

511 **3.3. Human subject MEG data**

512 Since the correct source locations for the human evoked field datasets are unknown, we plotted
513 the localization difference across the four LCMV implementations for each data. These localization
514 differences were the Cartesian distance between an LCMV-estimated source location and the
515 corresponding reference dipole location as explained in Section 2.2.3. Fig. 9a shows the plots for
516 the localization differences against the input SNRs computed using Eq (10) for four visual, two
517 auditory and two somatosensory evoked-field datasets. The localization differences for both
518 unprocessed raw and SSS preprocessed data are mostly under 20 mm in each toolbox. The higher

519 differences compared to the phantom and simulated dataset could be because of two reasons.
520 First, the recording might have been comprised by some head movement, which could not be
521 corrected because of the lack of continuous HPI information. Second, the reference dipole location
522 may not represent the very same source as estimated by the LCMV beamformer. In contrast to
523 dipole fitting, beamforming utilizes data from the full covariance window, so some difference
524 between the estimated localizations is to be expected. For all SSS-preprocessed evoked field
525 datasets, Fig. 9b shows the estimated locations across the four LCMV implementation and the
526 corresponding reference dipole locations. For simplifying the visualization, all estimated locations
527 in a stimulus category are projected onto a single axial slice. All localizations seem to be in the
528 correct anatomical regions, except the estimated location from right-ear auditory responses by
529 MNE-Python after SSS-preprocessing (Fig. 9b; red circle). This could be because of high
530 coherence between left-right auditory responses. After de-selecting the channels close to the right
531 auditory cortex, the MNE-Python-estimated source location was correctly in the left cortex (Fig. 9b;
532 green circle). Fig. 9a also shows the improvement in input SNR and also in the source localization
533 in some cases after SSS pre-preprocessing. Fig. 8 in Supplementary material shows the PSV
534 values as a function of the input SNR for the evoked-field datasets, demonstrating the spatial
535 resolution of beamforming.

536

537

Insert Fig. 9 about here

538

539

540

541

542 4. Discussion

543 In this study, we compared four widely-used open-source toolboxes for their LCMV beamformer
544 implementations. While the implementations share the theoretical basis, there are also differences,
545 which could lead to differing source estimates. There are also several other beamformer variants
546 (e.g. Huang et al., 2004; Cheyne et al., 2007; Herdman et al. 2018) but an extensive comparison of
547 all beamformer formulations would be a tedious task; however, most of our findings likely apply to
548 other formulations such as event-related beamformers, too.

549 We investigated the localization accuracy and beamformer resolution as a function of the input
550 SNR and compared the results across the LCMV implementations in the four tested toolboxes. In
551 the absence of background noise and using perfect sphere model, the phantom data showed high
552 localization accuracy and high spatial resolution if the input SNR $> \sim 5$ dB. All implementations also
553 showed high localization accuracy for data recording from a moving phantom after compensating
554 the movement and applying tSSS. For the simulated datasets with realistic background noise and
555 imperfect forward model, the localization errors across the LCMV implementations indicated that
556 the reliability of localization in these implementations depends on the SNR of input data.
557 Brainstorm (vector beamformer) reliably localized a single source when SNR was above ~ 3 dB,
558 including very high SNRs, whereas the other three implementations (scalar beamformer) localized
559 the source reliably within the SNR range of ~ 3 – 15 dB. Small deviations were observed in the
560 estimated source locations across the implementations even in this SNR range, likely caused by
561 differences in the pre-processing steps such as filter types, head models, spatial filter and
562 performing the beamformer scan. For the human evoked-response MEG data, all implementations
563 localized sources within about 20 mm from each other.

564 Our results indicate that with the default parameter settings, none of the four implementations
565 works universally reliable for all datasets and all input SNR values. In the case of low SNR
566 (typically less than 3 dB), the lower contrast between data and noise covariance may cause the
567 beamformer scan to provide a flat peak in the output and so the localization error goes high. The
568 unexpected high localization errors can be observed at some cases of high SNR signals for the
569 three scalar-type beamformer implementations and significant localization differences between the
570 toolboxes are notable. The PSV plots show greater spatial resolution for the SNR range ~ 3 – 15 dB
571 whereas low spatial resolution at very low and high SNR. Brainstorm provides reliable localization
572 above ~ 3 dB but it also compromises spatial resolution; see Fig. 6–7 and Table 2. The lower
573 spatial resolution (higher PSV) for the signal with low SNR also agrees with previous studies (Lin et
574 al., 2008; Hillebrand and Barnes, 2003).

575 For our simulated data, all toolboxes had a disparity between the forward model used in data
576 generation model and the model used in beamforming, i.e, the forward model was not perfect. The
577 width of the source estimate peak depends on both the SNR (van Veen et al., 1997; Vrba and

578 Robinson, 2000; Gross et al., 2001; Hillebrand and Barnes, 2003) and also on the type of
579 beamformer applied (scalar vs. vector). If the SNR is very high, the peak is also very narrow, and
580 any errors introduced by the forward model will be pronounced, leading to larger localization errors
581 of this peak. For unconstrained vector beamformers, the peak is comparatively broader (higher
582 PSV) and there is a smaller chance of missing the peak; this is the case with Brainstorm in our
583 study. In the following, we discuss the significant steps of the beamformer pipelines, which affect
584 the localization accuracy and introduce discrepancies among the implementations.

585 **4.1 Preprocessing with SSS**

586 Due to the spatial-filter nature of the beamformer, it can reject external interference and therefore
587 SSS-based pre-processing for interference suppression may have little effect on the results. Thus,
588 although the SNR increases as a result of applying SSS, the localization accuracy does not
589 necessarily improve, which is evident in the localization of the evoked responses (Fig. 9).

590 However, undetected artifacts, such as a large-amplitude signal jump in a single sensor, may in
591 SSS processing spread to neighboring channels and subsequently reduce data quality. Therefore,
592 channels with distinct artifacts should be noted and excluded from beamforming of unprocessed
593 data or from SSS operations. In addition, trials with large artifacts should be removed based on an
594 amplitude thresholding or by other means. Furthermore, SSS processing of extremely weak
595 signals (SNR < ~2 dB) may not improve the SNR for producing smaller localization errors and PSV
596 values. Hence the data quality should be carefully inspected before and after applying
597 preprocessing methods such as SSS, and channels or trials with low-quality data (or lower
598 contrast) should be omitted from the covariance estimation.

599 **4.2. Effect of filtering and artifact-removal methods**

600 All four toolboxes we tested employ either a MATLAB or Python implementation of the same MNE
601 routines (Gramfort et al. 2014) for reading FIFF data files and thus have internally the exact same
602 data at the very first stage (see Suppl. Fig. 6). The data import either keeps the data in SI-units (T
603 for magnetometers and T/m for gradiometers) or rescales the data (fT and fT/mm) before further
604 processing. The actual pre-processing steps in the pipeline may contribute to differences in the
605 results. The filtering step is performed to remove frequency components of no interest, such as
606 slow drifts, from the data. By default, FieldTrip and SPM use an IIR (Butterworth) filter, and MNE-
607 Python uses FIR filters. The power spectra of these filters' output signals show notable differences
608 and the output data from these two filters are not identical. Significant variations can be found
609 between MNE-Python-filtered and FieldTrip/SPM-filtered data. Although SPM12 and FieldTrip use
610 the same filter implementation, the filtering results are not identical because of numeric differences
611 caused by different channel units (Suppl. Fig 6). These differences affect the estimated covariance
612 matrices, which are a crucial ingredient for the spatial-filter computation and finally may contribute
613 to differences in beamforming results.

614 **4.3. Effect of SNR on localization accuracy**

615 We reduced the impact of the unknown source depth and strength to a well-defined metrics in
616 terms of the SNR. We observed that the localization accuracy is poor for very low SNR values, i.e.
617 below 3 dB. The weaker, as well as the deeper sources, project less power on to the sensor array
618 and thus show lower SNR; see Eq (10). On the other hand, the LCMV beamformer may also fail to
619 localize accurately sources that produce very high SNR, likely because the point spread of the
620 beamformer output becomes narrower than the distance between the scanning grid points. In this
621 case, the estimate is very focal and a small error in forward solution, introduced e.g. by inaccurate
622 coregistration, may lead to missing the true source and obtaining nearly equal power estimates at
623 many source grid locations, increasing the chance of mislocalization. Brainstorm produced a
624 different outcome at high SNR than the other toolboxes, because the vector beamformer in
625 Brainstorm has wider spatial peaks and thus the maximum NAI occurs more likely in one of the
626 source grid locations.

627 Such high SNRs do not typically occur in human MEG experiments. However, pathological brain
628 activity may produce high SNR, e.g. the strength of equivalent current dipoles (ECD) for modeling
629 sources of interictal epileptiform discharges (IIEDs) typically ranges between 50 and 500 nAm
630 (Bagic et al., 2011a).

631 **4.4. Effect of the head model**

632 Forward modelling requires MEG–MRI co-registration, segmentation of the head MRI and leadfield
633 computation for the source space. The four beamformer implementations use different
634 approaches, or similar approaches but with different parameters, which yields slightly different
635 forward models. From Eqs (3–8), it is evident that beamformers are quite sensitive to the forward
636 model. Hillebrand and Barnes (2003) showed that the spatial resolution and the localization
637 accuracy of a beamformer improve with accuracy of the forward model. Dalal and colleagues
638 (2014) reported that co-registration errors contribute greatly to EEG localization inaccuracy, likely
639 due to their ultimate impact on head-model quality. Chella and colleagues (2019) presented the
640 dependency of beamformer-based functional connectivity estimates on MEG-MRI co-registration
641 accuracy.

642 The increasing inter-toolbox localization differences towards very low and very high input SNR is
643 also subject to the differences between the head models. Fig. 4 shows the four overlapped source
644 space boundaries prepared from the same MRI where a slight misalignment among them can be
645 easily seen. This misalignment affects source space. Such differences in head models and source
646 spaces contribute differences in forward solutions which further will contribute to differences in
647 beamforming results across the toolboxes.

648 **4.5. Covariance matrix and regularization**

649 The data covariance matrix is a key component of the adaptive spatial filter in LCMV beamforming,
650 and any error in covariance estimation can cause an error in source estimation. We used 5% of the
651 mean variance of all sensors to regularize data covariance for making its inversion stable in
652 FieldTrip, DAiSS (SPM12) and MNE-Python. Brainstorm uses a slightly different approach and
653 applies regularization with 5% of mean variance of gradiometer and magnetometer channel sets
654 separately and eliminates cross-sensor-type entries from the covariance matrices. As SSS
655 preprocessing reduces the rank of the data, usually retaining less than 80 non-zero eigenvalues,
656 the trace of the covariance matrix decreases strongly. At very high SNRs (> 15 dB), overfitting of
657 the covariance matrix becomes more prominent; the condition number (ratio of the largest and the
658 smallest eigenvalues) of the covariance matrix becomes very high even after the default
659 regularization, which can deteriorate the quality of source estimates unless the covariance is
660 appropriately regularized. Therefore, the seemingly same 5% regularization can have very different
661 effects before and after SSS; see Suppl. Fig. 7. Thus, the commonly used way of specifying the
662 regularization level might not be appropriate to produce a good and stable covariance model at
663 high SNR, and this could be one of the explanations for the anecdotally reported detrimental
664 effects of SSS on beamforming results.

665 **5. Conclusion**

666 We conclude that with the current versions of LCMV beamformer implementations in the four open-
667 source toolboxes — FieldTrip, DAiSS (SPM12), Brainstorm, and MNE-Python — the localization
668 accuracy is acceptable (within ~ 10 mm for a true point source) for most purposes when the input
669 SNR is ~ 3 – 15 dB. Lower or higher SNR may compromise the localization accuracy and spatial
670 resolution. All toolboxes apply a vector LCMV beamformer as the initial step to find the source
671 location. FieldTrip, DAiSS (SPM12) and MNE-Python find the optimal source orientation and
672 produce a scalar beamformer output. Brainstorm yields robust localization for input SNR > 5 dB but
673 it slightly compromises with the spatial resolution.

674 To extend this useable range, a properly defined scaling strategy such as pre-whitening should be
675 implemented across the toolboxes. The default regularization is often inadequate and may yield
676 suboptimal results. Therefore, a data-driven approach for regularization should be adopted to
677 alleviate problems with low- and high-SNR cases. Our further work will be focusing on optimizing
678 regularization using a more data-driven approach.

679

680 **Acknowledgment**

681 This study has been supported by the European Union H2020 MSCA-ITN-2014-ETN program,
682 Advancing brain research in Children's developmental neurocognitive disorders project (ChildBrain
683 #641652). SSD and BUW have been supported by an ERC Starting Grant (#640448).

684

685 **References**

- 686 Bagic, A. I., Knowlton, R. C., Rose, D. F., Ebersole, J. S., & ACMEGS Clinical Practice Guideline
687 (CPG) Committee. (2011a). American clinical magnetoencephalography society clinical practice
688 guideline 1: recording and analysis of spontaneous cerebral activity. *J Clin Neurophysiol.* **28**(4):
689 348–354. <http://dx.doi.org/10.1097/WNP.0b013e3182272fed>
- 690 Bagic, A. I., Knowlton, R. C., Rose, D. F., Ebersole, J. S., & ACMEGS Clinical Practice Guideline
691 (CPG) Committee. (2011b). American Clinical Magnetoencephalography Society Clinical Practice
692 Guideline 3: MEG–EEG Reporting. *J Clin Neurophysiol.* **28**(4): 362–365.
693 <http://dx.doi.org/10.1097/WNO.0b013e3181cde4ad>
- 694 Barca, L., Cornelissen, P., Simpson, M., Urooj, U., Woods, W., & Ellis, A. W. (2011). The neural
695 basis of the right visual field advantage in reading: an MEG analysis using virtual electrodes. *Brain*
696 *Lang* **118**(3): 53–71. <http://dx.doi.org/10.1016/j.bandl.2010.09.003>
- 697 Burgess, R. C., Funke, M. E., Bowyer, S. M., Lewine, J. D., Kirsch, H. E., Bagić, A. I., & ACMEGS
698 Clinical Practice Guideline (CPG) Committee (2011). American Clinical Magnetoencephalography
699 Society Clinical Practice Guideline 2: Presurgical functional brain mapping using magnetic evoked
700 fields. *J Clin Neurophysiol.* **28**(4): 355–361. <http://dx.doi.org/10.1097/WNP.0b013e3182272ffe>
- 701 Chella, F., Marzetti, L., Stenroos, M., Parkkonen, L., Ilmoniemi, R. J., Romani, G. L., & Pizzella, V.
702 (2019). The impact of improved MEG–MRI co-registration on MEG connectivity analysis.
703 *NeuroImage*, **197**: 354-367. <https://doi.org/10.1016/j.neuroimage.2019.04.061>
- 704 Cheyne, D., Bostan, A.C., Gaetz, W., Pang, E.W. (2007) Event-related beamforming: A robust
705 method for presurgical functional mapping using MEG, *Clin. Neurophys.* **118**, 16911704.
706 <https://doi.org/10.1016/j.clinph.2007.05.064>
- 707 Dalal, S. S., Rampp, S., Willomitzer, F., & Ettl, S. (2014). Consequences of EEG electrode position
708 error on ultimate beamformer source reconstruction performance. *Front Neurosci.* **8**: 42.
709 <http://dx.doi.org/10.3389/fnins.2014.00042>
- 710 Dale, A. M., Fischl, B., & Sereno, M. I. (1999). Cortical surface-based analysis I: Segmentation and
711 surface reconstruction. *Neuroimage* **9**(2): 179-194. <https://doi.org/10.1006/nimg.1998.0395>
- 712 Dale, A. M., Liu, A. K., Fischl, B. R., Buckner, R. L., Belliveau, J. W., Lewine, J. D., & Halgren, E.
713 (2000). Dynamic statistical parametric mapping: combining fMRI and MEG for high-resolution
714 imaging of cortical activity. *Neuron* **26**(1): 55–67. [http://dx.doi.org/10.1016/S0896-6273\(00\)81138-1](http://dx.doi.org/10.1016/S0896-6273(00)81138-1)
- 715 Elekta Neuromag® TRIUX User's Manual, (Megin Oy, 2018)

- 716 Engemann, D. A., & Gramfort, A. (2015). Automated model selection in covariance estimation and
717 spatial whitening of MEG and EEG signals. *NeuroImage* **108**: 328–342.
718 <http://dx.doi.org/10.1016/j.neuroimage.2014.12.040>
- 719 Fischl, B. (2012). FreeSurfer. *Neuroimage* **62**(2): 774–781.
720 <https://doi.org/10.1016/j.neuroimage.2012.01.021>
- 721 Fischl, B., Sereno, M. I. & Dale, A. M. (1999). Cortical surface-based analysis II: Inflation,
722 flattening, and a surface-based coordinate system. *NeuroImage* **9**(2): 195–207.
723 <https://doi.org/10.1006/nimg.1998.0396>
- 724 Gramfort, A., Luessi, M., Larson, E., Engemann, D. A., Strohmeier, D., Brodbeck, C., ... &
725 Hämäläinen, M. (2013a). MEG and EEG data analysis with MNE-Python. *Front Neurosci.* **7**: 267.
726 <http://dx.doi.org/10.3389/fnins.2013.00267>
- 727 Gramfort, A., Strohmeier, D., Haueisen, J., Hämäläinen, M. S., & Kowalski, M. (2013b). Time-
728 frequency mixed-norm estimates: Sparse M/EEG imaging with non-stationary source activations.
729 *NeuroImage* **70**: 410–422. <http://dx.doi.org/10.1016/j.neuroimage.2012.12.051>
- 730 Gramfort, A., Luessi, M., Larson, E., Engemann, D. A., Strohmeier, D., Brodbeck, C., ... &
731 Hämäläinen, M. S. (2014). MNE software for processing MEG and EEG data. *Neuroimage* **86**:
732 446–460. <http://dx.doi.org/10.1016/j.neuroimage.2013.10.027>
- 733 Gross, J., Kujala, J., Hämäläinen, M., Timmermann, L., Schnitzler, A., & Salmelin, R. (2001).
734 Dynamic imaging of coherent sources: studying neural interactions in the human brain. *Proc Natl*
735 *Acad Sci USA* **98**(2): 694-699. <http://dx.doi.org/10.1073/pnas.98.2.694>
- 736 Hall, M. B., Nissen, I. A., van Straaten, E. C., Furlong, P. L., Witton, C., Foley, E., ... & Hillebrand,
737 A. (2018). An evaluation of kurtosis beamforming in magnetoencephalography to localize the
738 epileptogenic zone in drug-resistant epilepsy patients. *Clin Neurophysiol.* **129**(6): 1221–1229.
739 <http://dx.doi.org/10.1016/j.clinph.2017.12.040>
- 740 Hämäläinen, M., Hari, R., Lounasmaa, O. V., Knuutila, J., & Ilmoniemi, R. J. (1993).
741 Magnetoencephalography-theory, instrumentation, and applications to noninvasive studies of the
742 working human brain. *Rev Mod Phys* **65**: 413–497. <https://doi.org/10.1103/RevModPhys.65.413>
- 743 Hämäläinen, M. S., & Ilmoniemi, R. J. (1994). Interpreting magnetic fields of the brain: minimum
744 norm estimates. *Med Biol Eng Compt.* **32**(1): 35–42. <https://doi.org/10.1007/BF02512476>
- 745 Hämäläinen, M. S., & Sarvas, J. (1989). Realistic conductivity geometry model of the human head
746 for interpretation of neuromagnetic data. *IEEE Trans Biomed Eng.* **36**(2): 165–171.
747 <https://doi.org/10.1109/10.16463>

- 748 Herdman, A., Moiseev, A. & Ribary, U. (2018) Localizing Event-Related Potentials Using Multi-
749 source Minimum Variance Beamformers: A Validation Study. *Brain Topogr.* 2018 Jul;31(4):546-
750 565. <http://dx.doi.org/10.1007/s10548-018-0627-x>.
- 751 Hillebrand, A., & Barnes, G. R. (2003). The use of anatomical constraints with MEG beamformers.
752 *Neuroimage* 20(4): 2302–2313. <http://dx.doi.org/10.1016/j.neuroimage.2003.07.031>
- 753 Hillebrand, A., & Barnes, G. R. (2005). Beamformer analysis of MEG data. *Int Rev Neurobiol* **68**:
754 149–171. [http://dx.doi.org/10.1016/S0074-7742\(05\)68006-3](http://dx.doi.org/10.1016/S0074-7742(05)68006-3)
- 755 Huang, M. X., Mosher, J. C., & Leahy, R. M. (1999). A sensor-weighted overlapping-sphere head
756 model and exhaustive head model comparison for MEG. *Phys Med Biol.* **44**(2): 423-440.
757 <http://dx.doi.org/10.1088/0031-9155/44/2/010>
- 758 Huang, M.X., Shih, J.J., Lee, R.R., Harrington, D.L., Thoma, R.J., Weisend, M.P., ...& Canive, J.M.
759 (2004) Commonalities and Differences Among Vectorized Beamformers in Electromagnetic Source
760 Imaging. *Brain Topography* **16**(3): 139-158.
761 <http://dx.doi.org/10.1023/B:BRAT.0000019183.92439.51>
- 762 Ilmoniemi, R. J., Hämäläinen, M. S., & Knuutila, J. (1985). The forward and inverse problems in the
763 spherical model, in: Weinberg, H., Stroink, G. & Katila, T. (Eds.), *Biomagnetism: Applications and*
764 *Theory. Pergamon Press, New York, 278–282*
- 765 Ilmoniemi, R. J., & Sarvas, J. (2019). *Brain Signals: Physics and Mathematics of MEG and EEG.*
766 *MIT Press.*
- 767 Ishii, R., Canuet, L., Ishihara, T., Aoki, Y., Ikeda, S., Hata, M., ... & Iwase, M. (2014). Frontal
768 midline theta rhythm and gamma power changes during focused attention on mental calculation:
769 an MEG beamformer analysis. *Front Hum Neurosci.* **8**: 406.
770 <http://dx.doi.org/10.3389/fnhum.2014.00406>
- 771 Lin, F. H., Witzel, T., Zeffiro, T. A., & Belliveau, J. W. (2008). Linear constraint minimum variance
772 beamformer functional magnetic resonance inverse imaging. *Neuroimage* **43**(2): 297–311.
773 <http://dx.doi.org/10.1016/j.neuroimage.2008.06.038>
- 774 Litvak, V., Mattout, J., Kiebel, S., Phillips, C., Henson, R., Kilner, J., ... & Penny, W. (2011). EEG
775 and MEG data analysis in SPM8. *Comput Intell Neurosci.* **2011**.
776 <http://dx.doi.org/10.1155/2011/852961>
- 777 Mattout, J., Henson, R. N., & Friston, K. J. (2007). Canonical source reconstruction for MEG.
778 *Comput Intell Neurosci.* **2007**. <http://dx.doi.org/10.1155/2007/67613>
- 779 Mohamed, I. S., Otsubo, H., Ferrari, P., Sharma, R., Ochi, A., Elliott, I., ... & Cheyne, D. (2013).
780 Source localization of interictal spike-locked neuromagnetic oscillations in pediatric neocortical

- 781 epilepsy Clinical Neurophysiology, 124(8), 1517-1527.
782 <http://dx.doi.org/10.1016/j.clinph.2013.01.023>
- 783 Mosher, J. C., Lewis, P. S., & Leahy, R. M. (1992). Multiple dipole modeling and localization from
784 spatio-temporal MEG data. *IEEE Trans Biomed Eng.* **39**(6): 541–557.
785 <http://dx.doi.org/10.1109/10.141192>
- 786 Nenonen J, Nurminen J, Kicic D, Bikmullina R, Lioumis P, Jousmäki V, Taulu S, Parkkonen L,
787 Putaala M, Kähkönen S (2012). Validation of head movement correction and spatiotemporal signal
788 space separation in magnetoencephalography. *Clin Neurophysiol.* **123**(11): 2180–2191.
789 <http://dx.doi.org/10.1016/j.clinph.2012.03.080>
- 790 Nolte, G. (2003). The magnetic lead field theorem in the quasi-static approximation and its use for
791 magnetoencephalography forward calculation in realistic volume conductors. *Phys Med Biol.*
792 **48**(22): 3637. <http://dx.doi.org/10.1088/0031-9155/48/22/002>
- 793 Oostenveld, R., Fries, P., Maris, E., & Schoffelen, J. M. (2011). FieldTrip: open source software for
794 advanced analysis of MEG, EEG, and invasive electrophysiological data. *Comput Intell Neurosci.*
795 **2011**. <http://dx.doi.org/10.1155/2011/156869>
- 796 Pascual-Marqui, R. D., Michel, C. M., & Lehmann, D. (1994). Low resolution electromagnetic
797 tomography: a new method for localizing electrical activity in the brain. *Int J Psychophysiol.* **18**(1):
798 49-65. [https://doi.org/10.1016/0167-8760\(84\)90014-X](https://doi.org/10.1016/0167-8760(84)90014-X)
- 799 Robinson S.E., Vrba, J. (1998). Functional neuroimaging by synthetic aperture magnetometry
800 (SAM), in: Yoshimoto, T., Kotani, M., Kuriki, S., Karibe, H. & Nakasato, N. (Eds.), Recent
801 Advances in Biomagnetism. *Tohoku University Press, Japan*, 302–305.
- 802 Salmelin, R. (2010). Multi-dipole modeling in MEG, in: Hansen, P., Kringelbach, M. & Salmelin, R.
803 (Eds.), MEG: an introduction to methods. *Oxford university press*, 124–155.
804 <http://dx.doi.org/10.1093/acprof:oso/9780195307238.003.0006>
- 805 Sekihara, K., & Scholz, B. (1996). Generalized Wiener estimation of three-dimensional current
806 distribution from biomagnetic measurements. *IEEE Trans Biomed Eng.* **43**(3): 281-291.
807 <http://dx.doi.org/10.1109/10.486285>
- 808 Sekihara, K., Hild, K. E., & Nagarajan, S. S. (2006). A novel adaptive beamformer for MEG source
809 reconstruction effective when large background brain activities exist. *IEEE Trans Biomed Eng.*
810 **53**(9), 1755–1764. <http://dx.doi.org/10.1109/TBME.2006.878119>
- 811 Sekihara, K., & Nagarajan, S., S. (2008). Adaptive spatial filters for electromagnetic brain imaging.
812 *Springer Science & Business Media.* <https://doi.org/10.1007/978-3-540-79370-0>

- 813 Sekihara, K., Nagarajan, S. S., Poeppel, D., & Marantz, A. (2004). Asymptotic SNR of scalar and
814 vector minimum-variance beamformers for neuromagnetic source reconstruction. *IEEE Trans*
815 *Biomed Eng.* **51**(10): 1726–1734. <http://dx.doi.org/10.1109/TBME.2004.827926>
- 816 Spencer, M. E., Leahy, R. M., Mosher, J. C., & Lewis, P. S. (1992). Adaptive filters for monitoring
817 localized brain activity from surface potential time series. in: *Conference Record of the Twenty-*
818 *Sixth Asilomar Conference on Signals, Systems & Computers.* **1992**: 156-161.
819 <http://dx.doi.org/10.1109/ACSSC.1992.269278>
- 820 Stenroos, M., Hunold, A., & Haueisen, J. (2014). Comparison of three-shell and simplified volume
821 conductor models in magnetoencephalography. *NeuroImage* **94**: 337-348.
822 <https://doi.org/10.1016/j.neuroimage.2014.01.006>
- 823 Tadel, F., Baillet, S., Mosher, J. C., Pantazis, D., & Leahy, R. M. (2011). Brainstorm: a user-friendly
824 application for MEG/EEG analysis. *Comput Intell Neurosci.*, **2011**.
825 <http://dx.doi.org/10.1155/2011/879716>
- 826 Taulu, S., & Kajola, M. (2005). Presentation of electromagnetic multichannel data: the signal space
827 separation method. *J Appl Physics* **97**(12): 124905. <http://dx.doi.org/10.1063/1.1935742>
- 828 Tikhonov, A. N. (1963). Solution of incorrectly formulated problems and the regularization method.
829 *Soviet Math.*, **4**: 1035–1038.
- 830 van Es, M. W., & Schoffelen, J. M. (2019). Stimulus-induced gamma power predicts the amplitude
831 of the subsequent visual evoked response. *NeuroImage* **186**: 703-712.
832 <http://dx.doi.org/10.1016/j.neuroimage.2018.11.029>
- 833 van Klink, N., van Rosmalen, F., Nenonen, J., Burnos, S., Helle, L., Taulu, S., ... & Hillebrand, A.
834 (2017). Automatic detection and visualization of MEG ripple oscillations in epilepsy. *NeuroImage*
835 *Clin* **15**: 689–701. <https://doi.org/10.1016/j.nicl.2017.06.024>
- 836 Van Veen, B. D., & Buckley, K. M. (1988). Beamforming: A versatile approach to spatial filtering.
837 *IEEE ASSP Magazine* **5**(2): 4–24. <http://dx.doi.org/10.1109/53.665>
- 838 Van Veen, B. D., Van Drongelen, W., Yuchtman, M., & Suzuki, A. (1997). Localization of brain
839 electrical activity via linearly constrained minimum variance spatial filtering. *IEEE Trans Biomed*
840 *Eng.* **44**(9): 867–880. <http://dx.doi.org/10.1109/10.623056>
- 841 Vrba, J., Robinson, S.E., (2000). Differences between synthetic aperture magnetometry (SAM) and
842 linear beamformers, In: Nenonen, J., Ilmoniemi, R.J., Katila, T. (Eds.), *12th International*
843 *Conference on Biomagnetism, Helsinki Univ. of Technology, Espoo, Finland*, 681–684.

- 844 Wipf, D. P., Owen, J. P., Attias, H. T., Sekihara, K., & Nagarajan, S. S. (2010). Robust Bayesian
845 estimation of the location, orientation, and time course of multiple correlated neural sources using
846 MEG. *NeuroImage* **49**(1): 641–655. <http://dx.doi.org/10.1016/j.neuroimage.2009.06.083>
- 847 Youssofzadeh, V., Agler, W., Tenney, J. R., & Kadis, D. S. (2018). Whole-brain MEG connectivity-
848 based analyses reveals critical hubs in childhood absence epilepsy. *Epilepsy Res.* **145**: 102-109.
849 <http://dx.doi.org/10.1016/j.eplepsyres.2018.06.001>

Journal Pre-proof

	MNE-Python	FieldTrip	DAiSS (SPM12)	Brainstorm
Version	0.18	20190922	20190924	20190926
Data import functions	MNE (Python)	MNE (Matlab)	MNE (Matlab)	MNE (Matlab)
Internal units of MEG data	T, T/m	T, T/m	fT, fT/mm	T, T/m
Band-pass filter type	FIR	IIR	IIR	FIR
MRI segmentation	FreeSurfer	SPM8/SPM12	SPM8/SPM12	FreeSurfer/SPM8
Head model	Single-shell BEM	Single-shell corrected sphere	Single-shell corrected sphere	Overlapping spheres
Source space	Rectangular grid (5 mm), inside of the inner skull	Rectangular grid (5 mm), inside of the inner skull	Rectangular grid (5 mm), inside of the inner skull	Rectangular grid (5 mm), inside of the brain volume
MEG-MRI coregistration	Point-cloud co-registration and manual correction	3-point manual co-registration followed by ICP co-registration	Point-cloud co-registration using ICP	Point-cloud co-registration using ICP
Data covariance matrix	Sample data covariance	Sample data covariance	Sample data covariance	Sample data covariance
Noise normalization for NAI computation	Sample noise covariance	Sample noise covariance	Sample noise covariance	Sample noise covariance
Combining data from multiple sensor types	Prewhitening (full noise covariance)	No scaling or prewhitening	No scaling or prewhitening	Prewhitening (full noise covariance but cross-sensor-type terms zeroed)
Beamformer type	Scalar	Scalar	Scalar	Vector
Beamformer output	Neural activity index (NAI)	Neural activity index (NAI)	Neural activity index (NAI)	Neural activity index (NAI)

Table 1. Characteristics of the four beamforming toolboxes. The non-default settings of each toolbox are shown in bold. The toolbox version is indicated either by the version number or by the download date (yyyymmdd) from GitHub.

	SNR range (dB)	MNE- Python	FieldTrip	DAiSS (SPM12)	Brainstorm
Mean loc. error for SSS-pre-processed simulated data (mm)	< 3	24.9	44.9	49.6	26.3
	3–15	6.1	6.3	5.9	9.9
	> 15	9.5	13.3	13.9	12.9
Mean PSV for SSS- pre-processed simulated data (cm ³)	< 3	84.9	84.9	139.4	101.1
	3–15	4.6	6.8	11.7	14.0
	> 15	19.2	21.0	34.9	39.9
Mean loc. error for SSS-pre-processed phantom data (mm)	< 3	3.6	2.9	3.6	3.8
	3–15	3.3	3.1	2.2	3.4
	> 15	3.7	3.0	2.5	3.5
Mean PSV for SSS- pre-processed phantom data (cm ³)	< 3	38.0	28.1	34.3	56.5
	3–15	1.8	2.0	4.8	5.8
	> 15	10.1	8.0	11.6	17.5

Table 2. Mean localization error and mean PSV for simulated and static phantom data over the three ranges of signal-to-noise ratio.

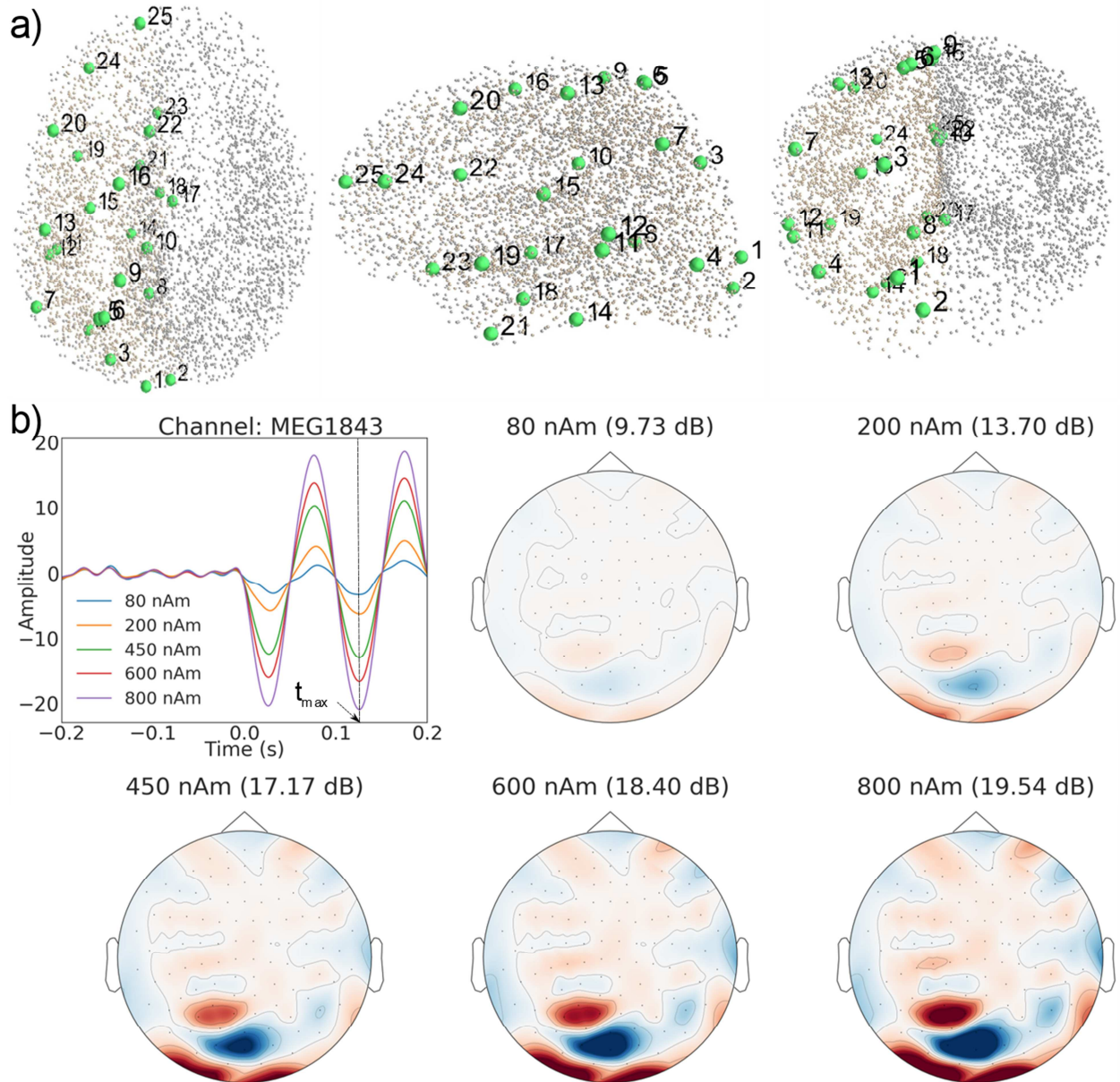


Fig. 1. Simulation of evoked responses. a) The 25 simulated dipolar sources (green dots) in the source space (grey dots), b) Simulated evoked responses of a dipolar source at five strengths and the field patterns corresponding to the peak amplitude (SNR in parenthesis). The dipole was located at $(-19.2, -71.6, 57.8)$ mm in head coordinates.

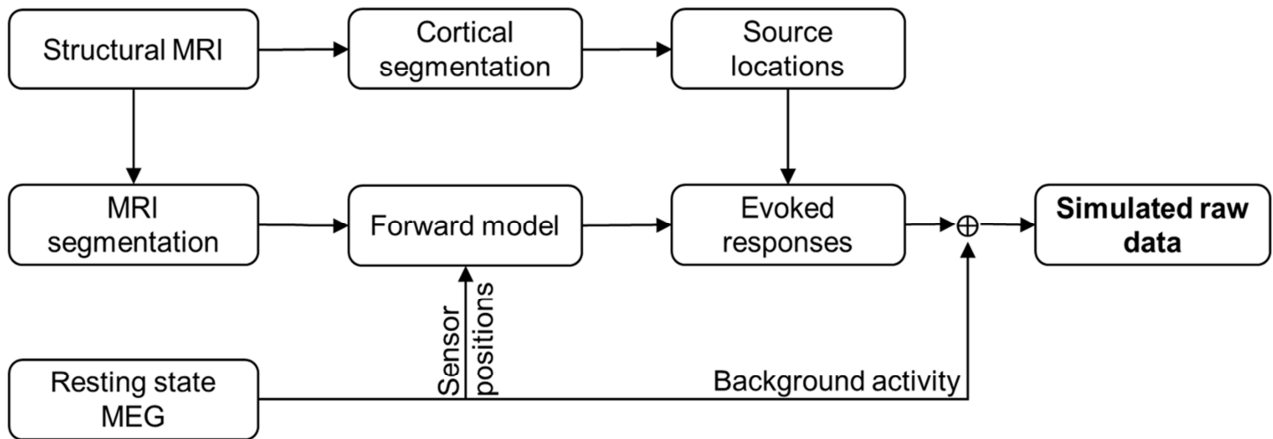


Fig. 2. MEG data simulation workflow (details in Suppl. Fig. 1).

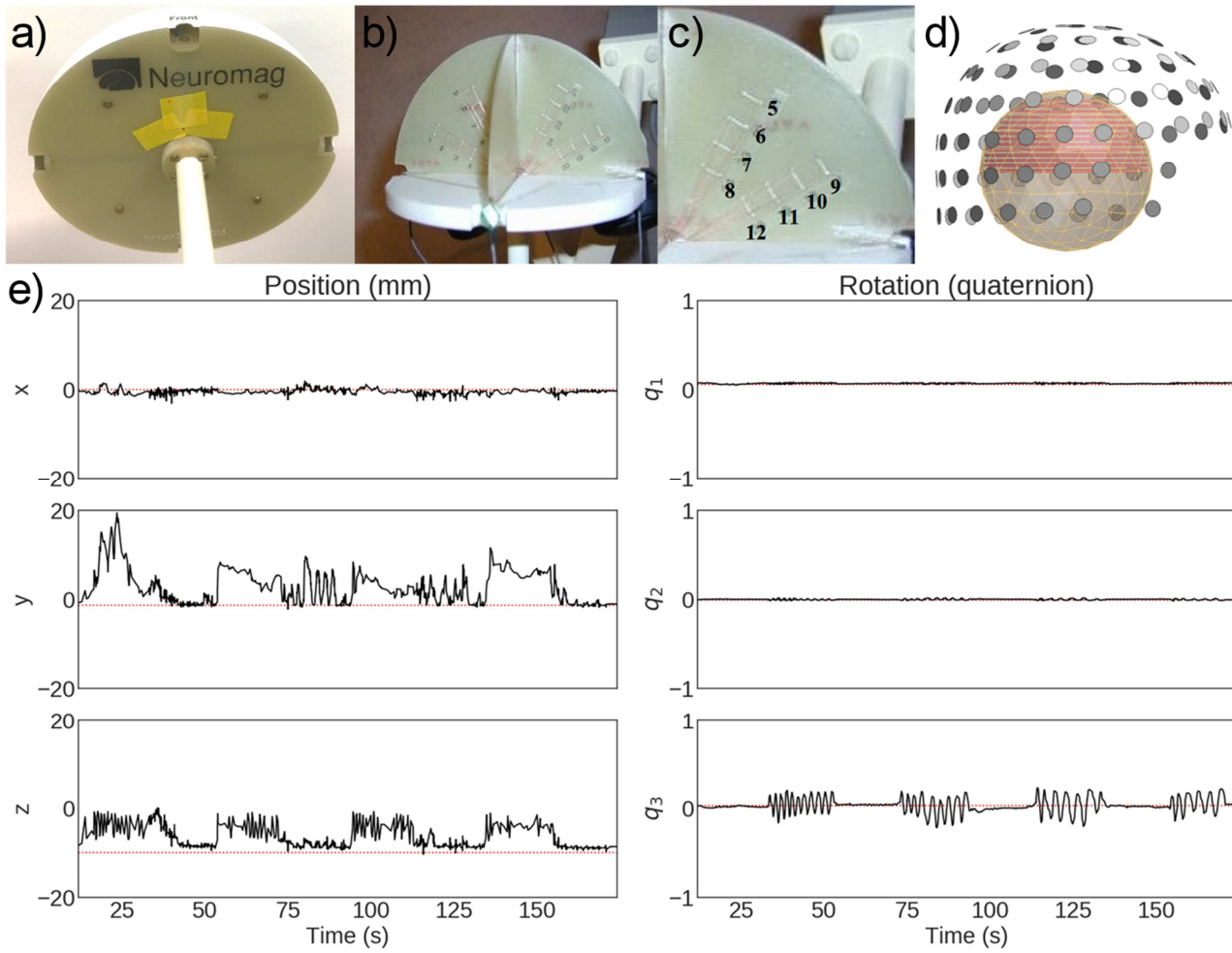


Fig. 3. The dry phantom. (a) Outer view, (b) cross-section, (c) positions of the employed dipole sources, (d) phantom position with respect to the MEG sensor helmet, and (e) position and rotation of the phantom during one of the moving-phantom measurements (Dipole 9 activated).

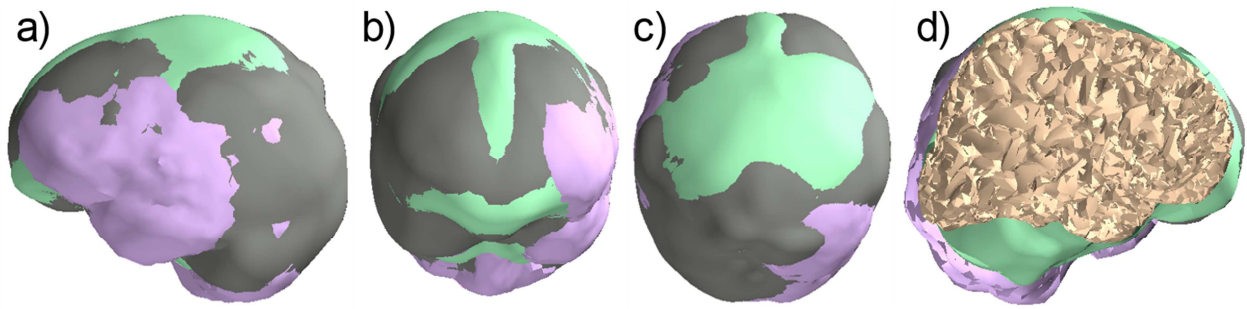


Fig. 4. Surfaces that bound the source space used by each toolbox. a) Sagittal, b) coronal, and c) axial views of the bounding surfaces in MNE-Python (grey), FieldTrip (lavender), DAiSS (SPM12) (mint) and Brainstorm (coral). d) Transparent view of the overlap and differences of the four surfaces (color indicates the outermost surface).

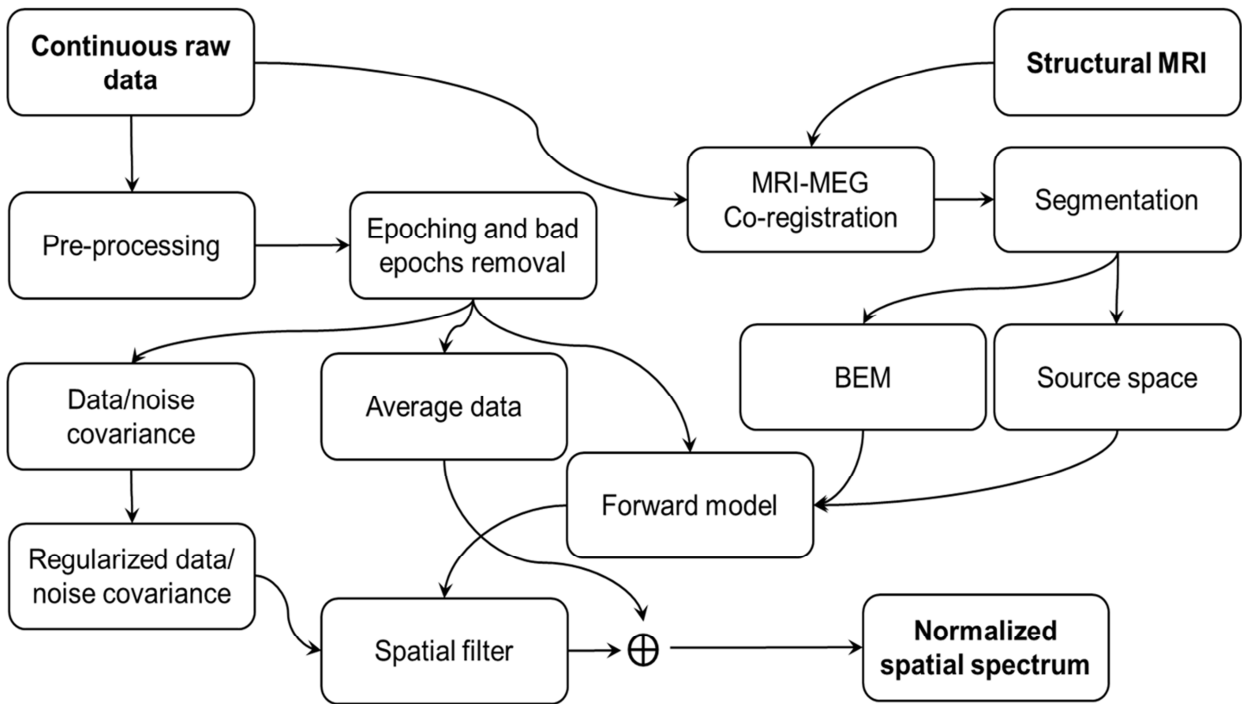


Fig. 5. The pipeline for constructing an LCMV beamformer for MEG/EEG source estimation. A similar pipeline was employed in all four packages.

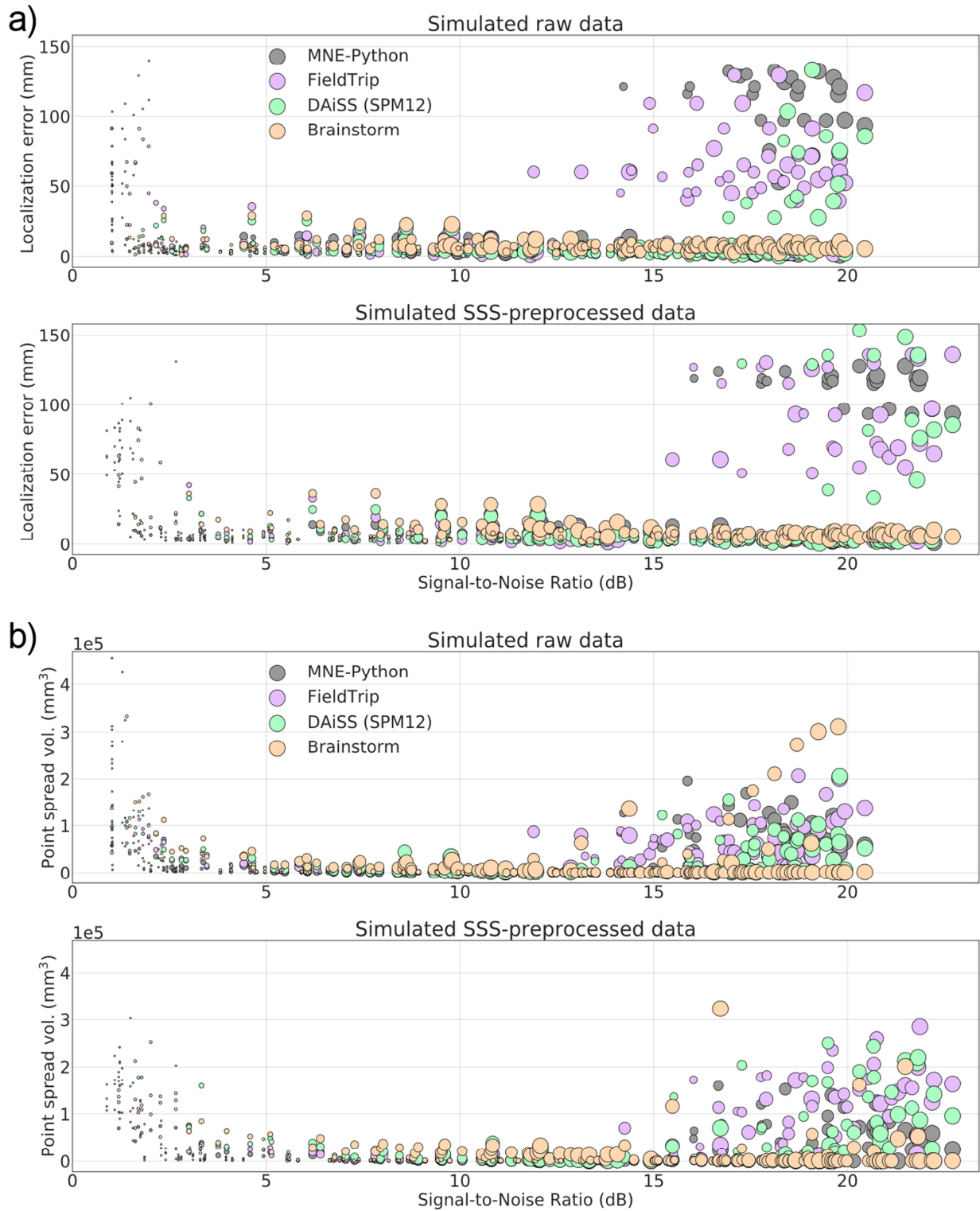


Fig. 6. Localization error (a) and point-spread volume (b) as a function of input SNR for raw and SSS-pre-processed simulated datasets. The markers size indicates the true dipole amplitude.

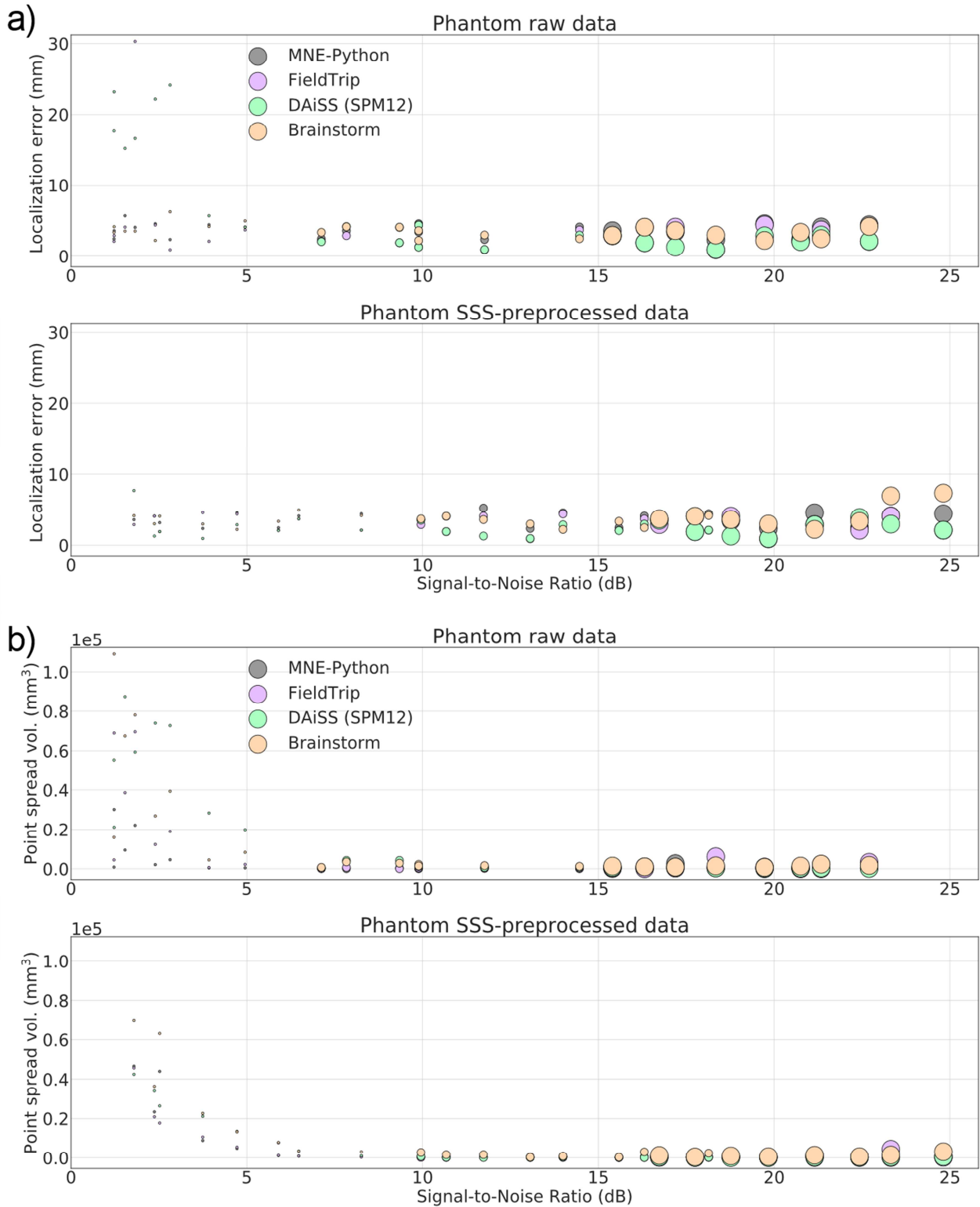


Fig. 7. Localization error (a) and point-spread volume (b) as a function of input SNR for phantom data recording in a stable position. The markers size indicates the true dipole amplitude.

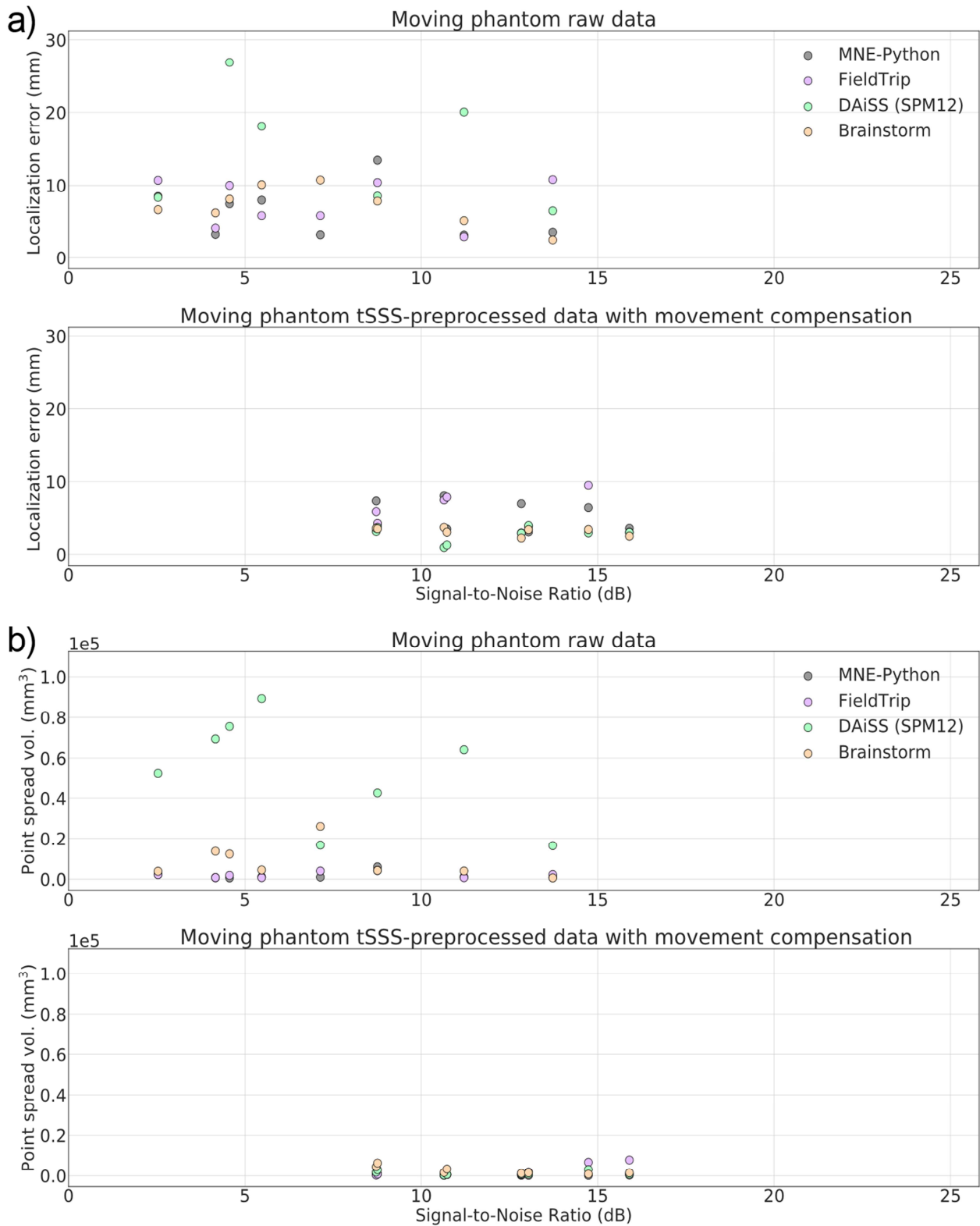


Fig. 8. Localization error (a) and point-spread volume (b) as a function of input SNR for data from the moving phantom.

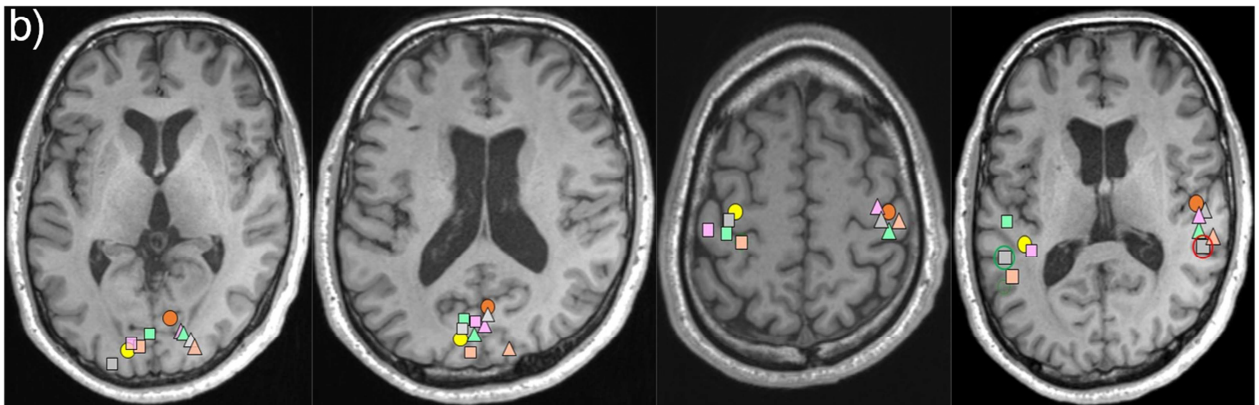
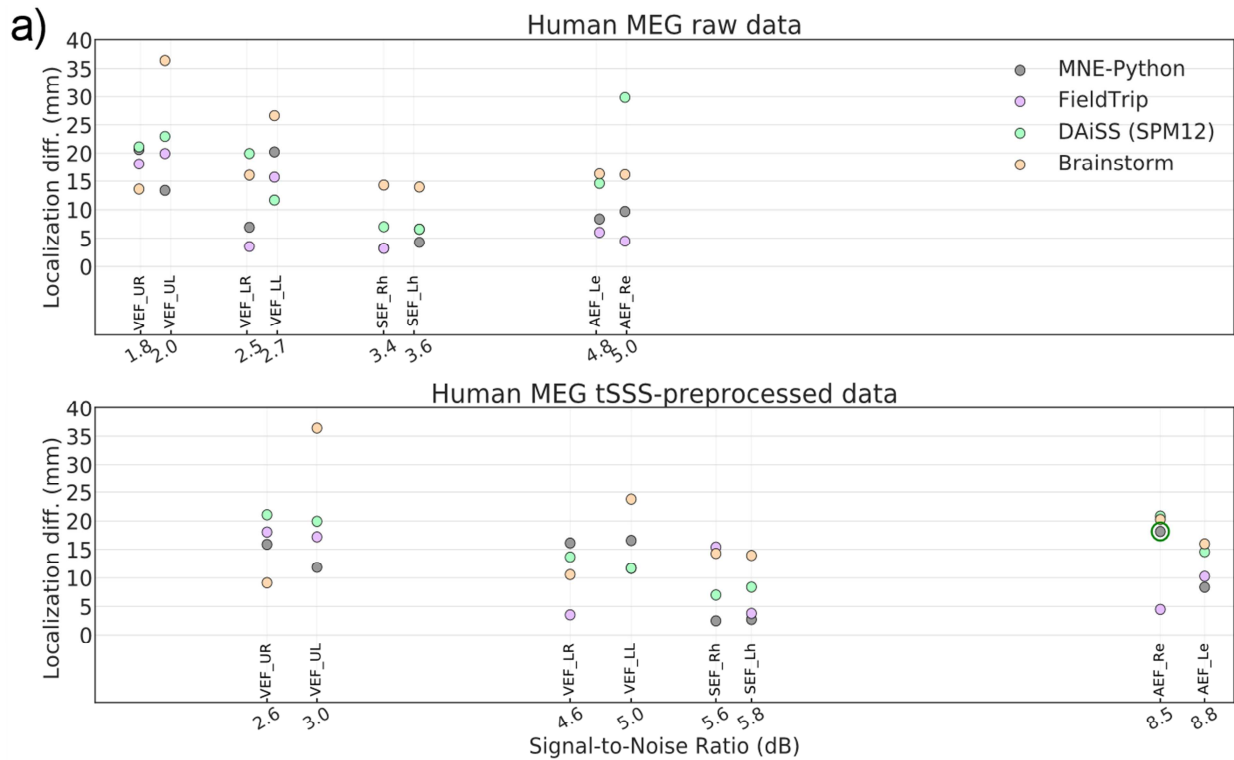


Fig. 9. Source estimates of human MEG data. (a) Localization difference from the reference dipole location for raw and tSSS-preprocessed data. (b) Peaks of the beamformer source estimate of tSSS-preprocessed data. From left to right: visual stimuli presented to left (triangle) and right (square) upper and lower quadrant of the visual field (the two axial slices showing all sources); somatosensory stimuli to left (triangle) and right (square) wrist; auditory stimuli to the left (triangle) and right (square) ear. Reference dipole locations (yellow and orange circles).

Credit Author Statement

- Amit Jaiswal:** Methodology, Software, Investigation, Writing- Original draft preparation,
Jukka Nenonen: Conceptualization, Data curation, Supervision, Reviewing and Editing
Matti Stenroos: Methodology, Reviewing and Editing
Alexandre Gramfort: Software (MNE-Python), Methodology
Sarang S. Dalal: Conceptualization, Reviewing and Editing
Britta U. Westner: Visualization, Reviewing and Editing
Vladimir Litvak: Software (SPM12), Reviewing and Editing
John C. Mosher: Methodology, Software (Brainstorm), Reviewing and Editing
Jan-Mathijs Schoffelen: Software (FieldTrip)
Caroline Witton: Validation, Supervision
Robert Oostenveld: Software (FieldTrip), Methodology
Lauri Parkkonen: Conceptualization, Methodology, Reviewing and Editing, Supervision